Flow visualization, heat transfer, and critical heat flux of flow boiling in Earth gravity with saturated liquid-vapor mixture inlet conditions – In preparation for experiments onboard the International Space Station

V.S. Devahdhanush[a], Steven J. Darges[a], Issam Mudawar[a,*], Henry K. Nahra[b], R. Balasubramaniam[b,c], Mohammad M. Hasan[b], Jeffrey R. Mackey[d]

[a] Purdue University Boiling and Two-Phase Flow Laboratory (PU-BTPFL), School of Mechanical Engineering, Purdue University, 585 Purdue Mall, West Lafayette, IN 47907, USA

[b] NASA Glenn Research Center, 21000 Brookpark Road, Cleveland, OH 44135, USA

[c] Case Western Reserve University, 10900 Euclid Ave., Cleveland, OH 44106, USA

[d] HX5, LLC, 3000 Aerospace Parkway, Brook Park, OH 44142, USA

Abstract – This study investigates flow boiling of n-Perfluorohexane with saturated two-phase mixture inlet in a rectangular channel of dimensions 114.6-mm heated length, 2.5-mm width, and 5 mm-height. The experiments were performed as part of the Mission Sequence Testing of the Flow Boiling and Condensation Experiment's (FBCE) Flow Boiling Module (FBM) in the vertical upflow configuration in Earth gravity using the same experimental system that was launched to the International Space Station (ISS) in August 2021. The operating parameters varied are heating configuration (single- and double-sided), mass velocity (380 – 2400 kg/m^{2}s), inlet quality (0.011 – 0.519), and inlet pressure (120 – 179 kPa). High-speed video photographs are presented to explain the two-phase flow patterns within the channel's heated length. Flow patterns are constituted by low-density and high-density fronts moving along the channel, with the high-density fronts gradually reducing in length due to evaporation. Heat transfer results in terms of flow boiling curves, streamwise wall temperature profiles, streamwise heat transfer coefficient profiles, and average heat transfer coefficients are presented and trends discussed. CHF data from the present experiments are combined with prior databases to compile a consolidated FBCE-CHF database for saturated inlet to expand the ranges of operating conditions and include other flow orientations in Earth gravity. Experimental CHF trends are also discussed. The interfacial lift-off model shows a good CHF predictive accuracy evidenced by a mean absolute error of 11.97% for this consolidated database after constraining it to mass velocities greater than or equal to 500 kg/m^{2}s. Finally, this study confirmed reliability of the upcoming ISS experiments for saturated inlet conditions and the collected Earth-gravity data will be compared to ISS microgravity data.

Keywords: flow boiling, saturated two-phase inlet, two-phase heat transfer coefficient, high-speed photography, critical heat flux, Earth gravity

* Author to whom correspondence should be addressed; Tel. (765) 494-5705; Fax (765) 494-0539; E-mail: *mudawar@ecn.purdue.edu;* Website: *https://engineering.purdue.edu/BTPFL*

Nomenclature

A	area; channel cross-sectional area
b	ratio of wetting front length to wavelength
C_1, C_2, C_3	constants
D	hydraulic diameter
f	friction factor
G	mass velocity
g	gravitational acceleration
g_e	gravitational acceleration on Earth
H	height of channel
H_{tc}	conduction distance through heating strip
h	enthalpy; heat transfer coefficient
$\overline{h}$	average heat transfer coefficient
h_{fg}	latent heat of vaporization
k	thermal conductivity; wave number
L_d	upstream development length
L_e	downstream exit length
L_h	heated length
$\dot{m}$	mass flow rate
N	number of data points
N_z	number of streamwise measurement locations
P	perimeter
p	pressure
q	total heat input
q''	heat flux
q''_{CHF}	critical heat flux
q''_{ONBD}	heat flux corresponding to ONBD
Re	Reynolds number
T	temperature
$\overline{T}$	average temperature
ΔT_{sub}	fluid subcooling, $\Delta T_{sub} = T_{sat} - T_f$
t	time
u	velocity
W	width of channel
x	flow quality
x_e	thermodynamic equilibrium quality

z	axial coordinate along flow direction
z_o	axial location where vapor velocity just exceeds liquid velocity
z^*	axial location for determining vapor layer thickness and critical wavelength

Greek symbols

α	void fraction
δ	mean vapor layer thickness
ε	thickness of liquid film on heated wall
λ	wavelength
μ	dynamic viscosity
μg_e	microgravity
ρ	density
ρ''	modified density
σ	surface tension
τ	shear stress
θ	orientation angle of channel
ξ_{15}	percentage of datapoints predicted within ±15%
ξ_{30}	percentage of datapoints predicted within ±30%

Subscripts

a	denotes wall 1 or 2 (= 1 or 2)
BHM	with respect to the BHM
c	critical
co	core
exp	experimental
f	saturated liquid; bulk fluid
g	saturated vapor
h	heated
i	interfacial
in	channel heated section inlet; inlet
k	either liquid (*f*) or vapor (*g*)
n	normal to heated wall
out	channel heated section outlet; outlet
pred	predicted
s	solid
sat	saturation

tc	thermocouple in heated strip
w	wall
wa	wall 1 or 2 (= *w*1 or *w*2)
z	local (along axial direction)

Acronyms

BHM	Bulk Heater Module
CHF	Critical Heat Flux
FBCE	Flow Boiling and Condensation Experiment
FBM	Flow Boiling Module
HDF	High-Density Front
ISS	International Space Station
LDF	Low-Density Front
MAE	Mean Absolute Error (%)
MST	Mission Sequence Testing
nPFH	n-Perfluorohexane
ONB	Onset of Nucleate Boiling
ONBD	Onset of Nucleate Boiling Degradation

1. Introduction

1.1 Two-phase Thermal Management in Future Space Missions

Future space missions planned by both NASA and other space agencies around the world are expected to be more powerful and for longer distances and durations. Thermal Control Systems (TCS) used in the space vehicles of such missions must be able to cater to the increased power dissipation requirements, while conserving both size and weight. Two-phase thermal management schemes involving boiling and condensation are best suited for such requirements as they utilize the coolant's enormous latent heat of vaporization in addition to sensible heating. Compared to single-phase schemes such as free and forced convection, two-phase schemes offer very high heat transfer coefficients and the ability to dissipate large amounts of heat while keeping the device at a safe low temperature. For several years, investigators at the Purdue University Boiling and Two-Phase Flow Laboratory (PU-BTPFL) have investigated numerous two-phase schemes such as capillary flows [1], evaporating falling films [2], flow boiling in macro-channels [3–6], micro-channels [5–7], and annuli [8], pool boiling [9,10], jet impingement boiling [11,12], spray cooling [13], and hybrid combinations thereof [14,15]. Each scheme has its own advantages and disadvantages, and must be carefully selected and optimized based on the application's

requirements. For space applications, channel flow boiling is preferred over the others due to its simplicity, dependence on flow inertia to remove the vapor produced along the heated surfaces, and adaptability to cool multiple devices in series in a fully closed loop while requiring relatively low pumping power. Another space application of two-phase schemes is in fission power systems coupled with the Rankine power cycle, which are characterized by enormous power-to-mass ratios and high thermal efficiencies [16,17].

1.2 Gravitational Effects on Heat Transfer and Flow Physics

Gravity has a substantial effect on two-phase flows due to the large difference in densities of the two phases. Space vehicles would be exposed to different gravity environments and hence the two-phase system must be designed to be suitable and adaptable for a wide range of gravities. A plethora of information exists on channel flow boiling in Earth gravity, but little is understood on its performance in microgravity, where the gravitational force is negligible and the flow physics is different.

Researchers have explored the effects of gravity on two-phase schemes by performing (i) Earth-gravity experiments at different flow orientations [18], (ii) short-duration microgravity (μg_e) experiments using drop towers [19,20], parabolic flights [20–24], and sounding/ballistic rockets [25], and (iii) longer-duration microgravity experiments onboard the International Space Station (ISS) [26]. However, most of these studies [23,24,26–28] have focused on pool boiling, which solely depends on buoyancy for liquid replenishment at the heated wall. The absence of buoyancy in μg_e produces a single large bubble on the heated surface, which severely degrades both heat transfer performance and Critical Heat Flux (CHF) value. Some μg_e studies [29,30] focused on adiabatic gas-liquid flows and observed that, of all the classical flow regimes, only the bubbly, slug, and annular flow regimes are prominently observed in μg_e. Very few μg_e flow boiling studies [20–22,31–35] exist in the literature, the experiments for which were performed for short μg_e durations. And among these, only Ohta [32] seems to have considered saturated two-phase mixture inlet of various qualities in the range of $x_{e,in} = 0 – 0.8$. Overall, a need exists to conduct long-duration flow boiling experiments in stable μg_e environments. In this regard, it is worth noting the parallel efforts by another group of researchers with the Japanese Aerospace Exploration Agency (JAXA) [36–38], whose experiments are on flow boiling of nPFH through 4-mm inner-diameter tubes made of heated copper and transparent heated glass (detailed research objectives are reported in [36]).

The three most important flow orientations experimented in Earth gravity are vertical upflow, vertical downflow, and horizontal flow, among which upflow is most stable and yields the highest heat transfer performance and CHF values, q''_{CHF}, due to buoyancy aiding in the removal

of produced vapor on the heated walls [39]. The present experiments are conducted in the vertical upflow orientation in Earth gravity and will serve as a forerunner to the upcoming μg_e experiments onboard the ISS.

1.3 Non-uniform Heating of Rectangular Channel

Most studies addressing the gravitational effects on flow boiling in rectangular channels were formulated by non-uniform heating of the channel walls. These consist of *single-sided heating* [40,41], where only one of the four walls is heated, and *double-sided heating* [21,42], where two opposite walls are heated. Both of these heating configurations help (i) isolate the effects of body force acting both perpendicular and parallel to the heated wall and (ii) simultaneously visualize the flow pattern evolution within the channel while heating. Between the two, single-sided heating helps understand the undisturbed evolution of the vapor layer along the heated wall, while double-sided heating introduces the effects of interfacial interaction between the two produced vapor layers. However, heating more than two walls would compromise flow visualization as well as inducing more three-dimensionality to the interfaces, and hence is not considered. Both the single- and double-sided heating configurations are tested in this study.

1.4 Saturated Inlet Conditions

In flow boiling, fluid enters the channel in either a subcooled or saturated state. Although subcooled liquid inlet is preferred for most thermal management applications owing to its augmented heat transfer performance, enhanced q''_{CHF}, and smaller pressure drop, saturated liquid-vapor mixture inlet is encountered in many situations. Most large-scale thermal management systems such as those in space vehicles are made of a single flow loop with several heat sources (loads) connected in series. Even though a two-phase system might be configured to have a subcooled liquid enter the first heat source, gradually with the absorption of more heat, the fluid becomes a saturated liquid-vapor mixture at some location along the flow loop. The latter heat sources would have saturated fluid entering them with various inlet qualities. Moreover, the inlet condition to the evaporator of a vapor compression heat pump and refrigeration system is two-phase with varying degree of vapor quality. Depending on the inlet quality, the heat transfer and fluid physics characteristics within the channel vary significantly. The interfacial flow patterns within the channel and the heat transfer mechanisms associated with each are greatly dependent on the inlet void fraction, which in turn is dependent on the inlet quality. Therefore, it is of equal importance to understand the physics of flow boiling with saturated inlet.

1.5 Critical Heat Flux for Saturated Two-Phase Inlet

CHF, which is the most important design parameter for flow boiling, is described to be either subcooled ($x_{e,out} < 0$) or saturated ($x_{e,out} \geq 0$) based on the fluid exit quality. Subcooled CHF is notorious for the non-equilibrium effects associated with it, especially when the exit fluid is highly subcooled. Subcooling has a less significant effect on saturated CHF to a point where, in some experiments using both single channels of 1.03, 2.20, and 3.04 mm diameter [43] and multi-channel heat sinks [44,45], inlet subcooling has been found to have a negligible effect on saturated CHF. The multi-micro-channel heat sink experiments of Mauro *et al*. [46] showed inlet subcooling to enhance q''_{CHF} only for R-134a and R-236fa, but had a negligible effect for R-245fa. Park and Thome's [47] multi-micro-channel heat-sink experiments showed inlet subcooling to moderately increase q''_{CHF} only for large inlet subcoolings (~20°C) in their largest channels (0.467 mm wide and 4.052 mm high).

On the other hand, saturated CHF with saturated two-phase inlet conditions poses its own unique challenges. The presence of an inlet void creates more complex flow patterns when compared to a pure liquid inlet. Konishi *et al*. [39] observed CHF at a variety of orientations for relatively low-quality saturated two-phase inlet flows. The vapor and liquid layers were found to remain separated when entering the channel and vapor production occur within the liquid layer along the heated wall. At low flow rates and unfavorable orientations such as downward facing heated walls, stratification of the phases was observed due to buoyancy. This resulted in the initial vapor layer insulating the heated wall along the entire channel length and prevented liquid access, yielding very low q''_{CHF}. Kharangate *et al*. [48] explored a wider range of qualities and noticed turbulent mixing of the vapor generated at the heated wall with the liquid-vapor mixture that entered the channel. The result was indistinct flow structures in the channel. Interestingly, for a fixed mass velocity, they discerned a non-monotonic trend of q''_{CHF} with respect to inlet quality with q''_{CHF} found to first increase then decrease with increasing quality. This was attributed, at relatively low qualities, to an increase in the velocity of each phase with increasing inlet quality. This effect was found to outweigh the effects of the additional vapor present in the channel downstream and resulted in larger q''_{CHF} for a wide range of flow rates. However, above a certain inlet quality (which depends on flow orientation, heating configuration, and other operating parameters), further increases negatively impacted q''_{CHF}. Tibirica *et al*. [49] performed flow boiling experiments using R-134a in a 0.38-mm-diameter 70-mm-long tube for inlet qualities of $x_{e,in}$ = -0.05 – 0.2 and G = 1400 kg/m^{2}s, and showed q''_{CHF} to be maximum for $x_{e,in}$ = 0.05. Ueda *et al*. [50] experimented flow boiling of R-113 through a vertical 10-mm-diameter circular channel of lengths 60 and 100 mm at $x_{e,in}$ = -0.06 – 0.62 and G = 357 – 1465 kg/m^{2}s. They found q''_{CHF} to monotonically decrease upon increasing $x_{e,in}$.

1.6 Objectives of Study

The present study is a crucial part of PU-BTPFL and NASA Glenn Research Center's ongoing collaborative effort to develop the Flow Boiling and Condensation Experiment (FBCE) for the International Space Station (ISS). As part of this effort, flow boiling experiments have already been performed both at different orientation in Earth gravity [42,48,51–54] and onboard an aircraft flying parabolic trajectories to simulate short microgravity periods [21,22,55]. Based on prior findings, a final refined experimental rig has been built and experimental test matrix and operating procedure determined for long-duration microgravity flow boiling experiments onboard the ISS. FBCE's capabilities, descriptions and photographs of the final system, and planned ISS test matrix are provided in [56].

Prior to launching to the ISS in August 2021, the final experimental system was used to perform certain pre-launch experiments (called Mission Sequence Testing, MST) in Earth gravity with the Flow Boiling Module (FBM) in the vertical upflow orientation. The MST experiments cover a sparsely-distributed subset of the planned ISS test matrix with different heating configurations, mass velocities, inlet qualities, and inlet pressures. With the experimental MST results for subcooled inlet already reported in [57,58], the present study covers those for saturated two-phase mixture inlet. High-speed video images are presented to explain the flow physics for various sets of operating conditions. Heat transfer results in terms of flow boiling curves, streamwise wall temperature profiles, streamwise heat transfer coefficient profiles, and average heat transfer coefficients are presented and explained. CHF results from the MST are combined with some older FBCE databases to form a consolidated saturated-inlet FBCE-CHF database and the interfacial lift-off model adopted to make predictions. Data from the present experiments will be compared against the upcoming ISS data to analyze the effects of gravity on flow boiling.

2. Experimental Methods

2.1 Two-Phase Flow Loop

A schematic of the experimental two-phase flow loop used to condition and supply the working fluid, n-Perfluorohexane (nPFH), to the Flow Boiling Module (FBM; the test module used in this study), is illustrated in Fig. 1. A magnetically-coupled internal gear pump positively displaces subcooled liquid nPFH through the flow loop. Two bypass relief valves of cracking pressures 199.95 kPa and 206.84 kPa are provided across the ends of the pump for safety, and they let fluid to pass from the pump outlet to pump inlet if the pressure differential exceeds the respective cracking pressure. Downstream of the pump, the fluid enters a Coriolis flow meter, wherein the flow rate is measured, and a filter, wherein any impurities are removed. Subcooled liquid enters the Bulk Heater Module (BHM; preheater), wherein it receives a predetermined

amount of heat from a set of heaters powered by Direct Current (DC), increases in temperature, and partially vaporizes. Thermocouples and Resistance Temperature Detectors (RTDs) within the BHM safely shut the heaters down in case either the temperature of the aluminum metal encasing the BHM heater core exceeds 130°C or the outlet fluid temperature exceeds 100°C. This saturated two-phase mixture enters the FBM, absorbs heat and increases in quality. The higher quality two-phase mixture is condensed back to subcooled liquid in a fluid-to-water stainless-steel tube-in-tube heat exchanger with a spiral-finned inner tube, by losing heat to the condensing water loop. A static mixer situated downstream of the condenser continuously mixes the liquid, condenses any possible vapor, and ensures thermodynamic uniformity. A highly subcooled pure liquid returns to the pump.

An accumulator is connected to the main loop at a T-junction downstream of the static mixer to help both maintain a set reference pressure at this location and reduce severe two-phase instabilities [59,60]. The section of the loop between the T-junction and pump is split into two parallel paths, one of which is used during regular experimentation and the other fitted with a degassing contactor used when degassing the fluid.

2.2 Flow Boiling Module

Schematics of the overall construction of the FBM are illustrated in Fig. 2(a) and key dimensions provided in Table 1. The FBM is primarily constructed using three transparent Zelux-W polycarbonate plates of respective thicknesses 25.15, 5.00, and 25.15 mm sandwiched between two 13.72-mm-thick aluminum support plates. A 5.0-mm deep and 2.5-mm wide slot is made in the middle polycarbonate plate to form the flow channel and two-oxygen-free copper heating strips of dimensions 114.6-mm length, 15.5-mm width, and 1.04-mm thickness are placed on either side of the slot. The fluid enters the FBM at a 90° angle to the flow channel, passes through an upstream 327.7-mm-long development length affixed with a 12.19-mm-thick aluminum honeycomb flow straightener close to the inlet, a middle 114.6-mm-long heated length, and a downstream 60.7-mm-long exit length, and finally exits the FBM at another 90° angle.

One side of the heating strips is in contact with the fluid and serves as heating wall, while to the other side are affixed a set of six thick-film resistors with a small separation between them to allow for heated-strip thermocouple access (see Fig. 2(b)). The heaters are wired in parallel and a maximum power of 175 W can be supplied independently to each strip so that both single- and double-sided heating configurations can be experimented. This heated wall design allows for fast temperature response and accurate CHF measurement [21,55].

2.3 Instrumentation and Measurement Accuracy

As illustrated in Fig. 1, local pressures are measured using absolute pressure transducers at five locations within the FBM: inlet, outlet, and three intermediary locations within the development length. In this study, the local pressure immediately upstream of the heated length is reported as p_{in} and that near the outlet as p_{out}. Fluid temperatures close to the inlet and outlet are measured using type-E thermocouples. As shown in Fig. 2(c), local temperatures of each heating strip are measured at seven equidistant locations using two sets of seven type-E thermocouples. One set is used for data collection and software reset of FBM heater power level in case any temperature exceeds 122°C, usually an aftermath of CHF. The other set is part of a hardware safety circuitry and provides feedback to a relay that shuts down the FBM heaters in case any temperature exceeds 132°C due to software-reset failure. Local pressures and temperatures at several points of the flow loop are respectively measured using pressure transducers, and thermocouples and RTDs. Both the voltages and currents to each set of FBM and BHM heaters are directly measured using a data acquisition system (DAQ). Flow rate is measured using a Coriolis flow meter of range 0-60 g/s. All temporal sensor output signals are collected and recorded using a set of two DAQs at a sampling frequency of 5 Hz and an in-house FBCE flight software is used to monitor and control the DAQs and other instruments.

Maximum measurement uncertainties of important parameters are listed in Table 2. Note that the actual value of CHF, q''_{CHF}, is determined as the average of the heat flux increment causing the 122°C strip temperature escalation and the preceding heat flux increment that reached steady state. This yields a CHF isolation error (difference between the true q''_{CHF} and the q''_{w} which triggered CHF) of ~1 W/cm^2 for majority of cases. However, some cases had slightly higher heat flux increases that provoked CHF; in these cases, CHF isolation error still remained below 2 W/cm^2.

2.4 Flow Visualization

High-speed video photography techniques are used to visualize the flow features within the heated section of the FBM. The rectangular channel's height is significantly greater than its width (heated) to effectively capture clear images through a thin slice of flow; a smaller width means fewer bubbles and clearer wavy interfaces through the imaging depth; a larger height makes possible a better study of bubble boundary and vapor layer development effects on each heated wall, and during double-sided heating, the clear interaction between vapor layers produced along both walls. The high-speed camera is directed at one transparent wall, while the other wall is backlit with blue light emitting diodes (LEDs) through an intermediate Teflon sheet serving as a light-shaping diffuser. The camera is equipped with a F#0.95-25 mm lens and captures photographs of resolution 2040×164 pixels at a frame rate of 2000 frames/s and shutter speed of

10 μs. All flow visualization images reported in this paper have been uniformly post-processed to make flow features more distinct.

2.5 Operating Procedure

As already mentioned, this study reports and analyzes results from the MST (the final set of pre-launch experiments in Earth gravity), the experimentation for which was remotely done in the same manner as will be onboard the ISS. The working fluid is degassed before the start of testing and as needed thereafter. Boiling curves for all predetermined operating conditions are obtained by setting each set of flow rates, inlet pressures, and BHM powers, and the system allowed to reach steady state. For each boiling curve, power to the FBM heaters is increased from a predetermined low power level until CHF is reached. Each heat flux increment is for a fixed time period of 120 – 180 s, which was deemed sufficient to reach steady state for flow boiling in prior studies with similar system designs [21,55]. For safety, if one of the strip thermocouples exceeds 122°C following CHF, the software automatically brings down the FBM heater power level to a minimum. If the software fails and any temperature exceeds 132°C, a redundant hardware shutdown of the heaters is invoked. Temporal data is recorded for entire boiling curves and high-speed photos taken towards the end of each heat flux increment.

More details on the experimental methods are provided in the authors' previous article [57].

2.6 Data Processing, Heat Loss Estimation, and Experimental Ranges

Steady-state datapoints corresponding to all heat flux increments that reached steady state, are extracted by averaging the latest 20 s of recorded temporal data of each steady-state period. All thermophysical properties of nPFH are obtained from NIST-REFPROP [61]. The fluid enthalpy at BHM (preheater) inlet is directly determined as

$$h_{BHM,in} = h\big|_{T_{BHM,in},\,p_{BHM,in}}, \tag{1}$$

where $T_{BHM,in}$ and $p_{BHM,in}$ are the BHM inlet fluid temperature and pressure, respectively. Per an energy balance over the BHM, the fluid enthalpy at BHM outlet is calculated as

$$h_{BHM,out} = h_{BHM,in} + \frac{q_{BHM}}{\dot{m}}, \tag{2}$$

where q_{BHM} is total BHM heat input and $\dot{m}$ mass flow rate through the flow loop.

The net heat loss upstream of the FBM heated section inlet (which is comprised of losses within the BHM, the flow path between the BHM and FBM, and the upstream development length with the FBM) is estimated by considering the MST experiments with both near-saturated inlet ($0 < \Delta T_{sub,in} < 10$°C) and visual confirmation of no vapor at FBM inlet for two reasons: (i) BHM

operation is similar for both the near-saturated and saturated inlet cases and heat loss values would be similar and (ii) to ensure complete thermodynamic equilibrium and pure liquid at FBM inlet for the single-phase calculations to be applicable. Percentage heat losses are estimated by comparing the measured heat input, which is q_{BHM}, and the actual net heat gain calculated by the enthalpy difference between the BHM inlet ($h_{BHM,in}$) and FBM heated section inlet (h_{in}), at which locations, the fluid state is subcooled liquid. Here, h_{in} is directly estimated using the measured pressure at the inlet of the heated section (p_{in}) and the measured fluid temperature (T_{in}) at the inlet of the FBM. It is found that, of all parameters, $\dot{m}$ dictates the heat loss percentages the most, and the best statistical fit yields the function $\%q_{net,loss} = 0.700\dot{m}^{-0.680}$. At very low flow rates, percentage heat losses are large, resulting in large uncertainties in estimating FBM enthalpy and quality at the inlet of the heated section. For instance, although experiments were conducted for $\dot{m} \approx 2.25$ g/s ($G \approx 180$ kg/m^{2}s), these cases are not considered in this study. It is noted that, with more experiments, a more robust heat loss estimation will be done for the upcoming ISS data. After subtracting estimated net heat losses from the measured q_{BHM} in Eq. (2), the fluid enthalpy at the FBM heated section inlet is determined as $h_{in} = h_{BHM,out}$.

Heat losses within the FBM's heated section were estimated to be within the heater power measurement uncertainty and are considered negligible [18,57]; so wall heat flux, q''_w, is calculated by dividing the electrical power input to the resistors by the fluid heating surface area. Per another energy balance over the FBM, the fluid enthalpy at FBM outlet is calculated as

$$h_{out} = h_{in} + \frac{q''_w P_h L_h}{\dot{m}}, \tag{3}$$

where P_h is heated perimeter determined from channel width, W, as

$$P_h = \begin{cases} W, & \text{single-sided heating} \\ 2W, & \text{double-sided heating} \end{cases}. \tag{4}$$

Thermodynamic equilibrium qualities at the FBM inlet and outlet are determined from the relation

$$x_e = \frac{h - h_f\big|_p}{h_{fg}\big|_p}, \tag{5}$$

where $h = h_{in}$ or h_{out} is the actual fluid enthalpy at FBM inlet/outlet, and both h_f, saturated liquid enthalpy, and h_{fg}, latent heat of vaporization, are based on the measured inlet/outlet pressure.

The measured heated-strip temperatures, T_{tc}, are translated into the corresponding wall temperatures, T_w, by assuming a uniform heat flux and one-dimensional heat conduction through the copper strip as

$$T_w = T_{tc} - \frac{q''_w H_{tc}}{k_s}, \tag{6}$$

where H_{tc} (= 0.483 mm) is the conduction height and k_s the pure copper conductivity. T_w is found to be lower than T_{tc} by a maximum of 0.37°C, indicating that the copper conductive resistance between the two points is minuscule and well within the T_{tc} measurement uncertainty. As shown in Fig. 2(c), local wall temperatures are designated as $T_{wa,z}$, where the subscript *wa* is the heated wall (*w*1 or *w*2) and *z* is the streamwise measurement location (1 upstream through 7 downstream).

The fluid being a saturated two-phase mixture throughout the FBM, the local fluid temperature at these axial locations, $T_{f,z}$, are equal to the local saturation temperatures, $T_{sat,z}$, estimated by linear interpolation between values at the inlet and outlet. Local heat transfer coefficient for either wall is defined as

$$h_{a,z} = \frac{q''_{wa}}{T_{wa,z} - T_{f,z}}, \tag{7}$$

and averaged heat transfer coefficient determined as

$$\overline{h} = \frac{\sum_{N_z} h_{a,z} A_{h,z}}{A_h} = \frac{\sum_{N_z} h_{a,z} L_{h,z}}{L_h}, \tag{8}$$

where N_z = 7 is the number of streamwise measurement locations, $A_{h,z}$ and $L_{h,z}$ are the heated surface area and length of each unit cell respectively, and A_h and L_h are the total heated surface area and total heated length respectively. Averaged wall temperature, $\overline{T_w}$, is also determined in a similar fashion. Ranges of important parameters from the MST experimental database with saturated inlet are reported in Table 3 for single- and double-sided heating configurations separately.

2.7 Temporal Temperature Records for an Entire Boiling Curve

Temporal records of fluid inlet, fluid outlet, and heated-strip temperatures are shown in Fig. 3 for a representative saturated-inlet boiling curve. The temperatures correspond to the left axis and the corresponding FBM wall heat fluxes to the right axis. Due to a relatively large FBM pressure drop and the fluid being saturated all along the flow channel, the outlet fluid temperature (which would be equal to the outlet saturation temperature) is consistently lower than the inlet fluid temperature. This means that, as heat flux is increased to reach q''_{CHF}, T_{in} slightly increases from 71.22 to 73.31°C due to a respective inlet pressure increase from 152.40 to 168.56 kPa, and T_{out} respectively increases from 67.55 to 69.37°C. Note that the parameter values included within the inset in Fig. 3 and other subsequent figures denotes the average ± standard deviation corresponding to all the data presented in the figure. For all heat flux increments preceding CHF, the strip temperatures, T_{tc}, clearly reach steady state. For the lowest two heat flux increments, *i.e.*, until about t = 300 s, the strip temperatures fall between the inlet and outlet fluid temperatures, meaning that axial conduction along the copper heating strips causes its temperature to be almost

uniform along their lengths. This means that more heat dissipation to the fluid occurs from the downstream portion of the channel; these low heat transfer cases would locally yield non-physical heat transfer coefficients and are excluded from data analysis. For $t > 300$ s, all T_{tc} are higher than the fluid temperature throughout the channel and the local variations in T_{tc} are due to the local two-phase flow regime at those measurement locations. During the last heat flux increment, at $t \approx 1690$ s, $T_{tc1,6}$ reaches the set maximum operating temperature of 122°C and the heaters are powered down. Note how the slopes of the T_{tc} curves, especially $T_{tc1,6}$, significantly changes towards the end, clearly indicative of CHF.

Overall, the temporal temperature records corroborate that (i) all heat flux increments preceding CHF clearly reach steady state within 120 – 180 s and (ii) CHF manifestation is indeed the cause of at least one strip temperature exceeding 122°C.

2.8 Miscellaneous Observations during Experimentation

During the MST experiments, some deviations from the predetermined set of operating conditions were observed. One such observation was the difficulty in maintaining a saturated inlet with a very low inlet quality all along the boiling curve, especially at high mass velocities. The variations of measured fluid temperature, measured pressure, and corresponding saturation temperature at the heated section inlet with increasing heat flux until CHF are shown in Fig. 4 for a set of operating conditions. Note that $G = 2400$ kg/m^{2}s is the highest mass velocity tested. Due to an increase in pressure drop in the flow loop with increasing heat flux, the mass flow rate controller increases the pressure at the pump head exit to maintain the set constant mass flow rate. As a result, p_{in} increases with increasing q''_w along the boiling curve; note how the average p_{in} is 182.28 kPa and the standard deviation is relatively large at 8.91 kPa. This increase in pressure results in an increase in the inlet saturation temperature, $T_{sat,in}$, from 71.94 to 77.20°C. But the measured inlet temperature to FBM remains almost a constant at $T_{in} = 72.54$°C, with a standard deviation of just 0.26°C. As indicated in Fig. 4, the T_{in} and $T_{sat,in}$ curves crossover at a certain heat flux, meaning that although the inlet was saturated at the beginning of this boiling curve, it ended up being subcooled (*near-saturated* to be precise) and CHF occurred with an inlet subcooling of $\Delta T_{sub,in} = 4.25$°C and an inlet quality of $x_{e,in} = -0.06$. Such cases were excluded from further analysis in this study.

3. Flow Visualization Results and Discussion

3.1 Flow Patterns for Single-sided Heating

A schematic representation of single-sided heating configurations is shown in Fig. 5(a). Flow is oriented vertically upwards fully opposing gravity and heat is added to one of the two

walls. Figures 5(b) and 5(c) portray flow patterns along the boiling curve for respective saturated inlet qualities of $x_{e,in}$ = 0.518 with right wall heated and 0.143 with left wall heated at the same mass velocity of $G \approx 790$ kg/m^{2}s. Included for each set of operating conditions are high-speed video images taken at steady state for heat fluxes ranging from the lowest tested until (and including) CHF. The wall heat flux, q''_w, corresponding to each image is mentioned right below it as a percentage of the respective q''_{CHF} for those operating conditions. As will be discussed in a later section, flow behavior at steady state is periodic and the images shown here are ones that best portray the time-averaged flow regime exhibited during that period.

The images for saturated inlet are complicated due to imaging through a highly chaotic liquid-vapor mixture with larger turbulence, larger three-dimensionality and highly disturbed interfaces (to the contrary, the images for subcooled inlet showed clear flow patterns with distinct interfacial features [57]). However, by careful observation and analysis, useful information can be gained, and conclusions reached. In Fig. 5(b), at a heat flux of 12.83% q''_{CHF}, the entire channel is mostly filled with a light region with some interspersed small dark regions. These light regions correspond to vapor-abundant regions or *low-density fronts* (LDF), which allow for more backlight transmission, and the dark regions to liquid-abundant regions or *high-density fronts* (HDF), which reduce the transmissibility of light. It may be easier for the reader to compare and visualize the HDFs as the liquid slugs observed in the classical slug flow regime and the LDFs the elongated bubbles. It is expected of a high $x_{e,in}$ of 0.518 to be largely vapor within the channel due to the overall dominance of the annular flow regime. To enable easy comparison between the different heat fluxes, all images in Fig. 5(b) are chosen such that a high-density front is aligned a short distance from the channel inlet. Visually, no significant differences can be detected between the various heat fluxes, indicating that wall heat flux has a negligible effect on flow patterns. Even the image corresponding to CHF does not show any distinguishable feature, meaning that the CHF mechanism for saturated inlet is more complex than for subcooled inlet.

Figure 5(c) is for the same mass velocity as in Fig. 5(b), but a lower inlet quality of $x_{e,in}$ of 0.143 and the left wall heated. The most striking aspect is the overall darker images due to the lower inlet quality and the presence of more liquid. The high-density fronts are longer than before. But again, as before, there are negligible differences between the images for different heat fluxes. Although both Figs. 5(b) and 5(c) are for single-sided heating at either opposite wall, there are no flow pattern biases across the channel centerline. The one feature that is not readily apparent amidst all the turbulence and chaos is the nucleation of small bubbles within the annular liquid film on the heated wall; if observed closely, these bubbles are seen to coalesce, form a vapor layer, and slide along the wall with the bulk flow. This behavior can be vaguely seen in Fig. 6, which presents a zoomed-in image sequence of the downstream portion of the channel at CHF for the

same case as in Fig. 5(c). Note the thin vapor layer next to the heated left wall and how the liquid-vapor interface has lifted-off the wall. It is hypothesized that this phenomenon plays a vital role in the CHF mechanism, but no conclusions can be reached with this limited evidence.

3.2 Flow Patterns for Double-sided Heating

A schematic representation of the double-sided heating configuration is shown in Fig. 7(a). Again, the flow is oriented vertically upwards fully opposing gravity, and both of the opposite walls are heated. Flow patterns along the boiling curve are portrayed in Figs. 7(b) and 7(c) for respective saturated inlet qualities of $x_{e,in} = 0.401$ at $G \approx 500$ kg/m^{2}s and 0.129 at $G \approx 1200$ kg/m^{2}s. In Fig. 7(b), the images are predominantly light characterized by mostly vapor, but with interspersed short dark liquid-abundant regions. Again, a high-density front is lined up at a short distance downstream of the inlet to enable better comparison, and there are no significant differences between the different heat fluxes. The HDFs here are longer and darker than in Fig. 5(b) due to the relatively lower inlet quality. As expected, similar to how Fig. 5(c) is darker than 5(b), Fig. 7(c) is darker than 7(b) due to the much lower inlet quality. Mass velocity does not seem to significantly affect the flow patterns, but largely controls the speed at which the high-density and low-density fronts move through the channel. Upon comparing the single- and double-sided heating configurations in Figs. 5 and 7, heating configuration does not seem to play a role in determining the flow patterns for this channel geometry and operating conditions.

Overall, flow patterns are largely dependent on the inlet quality, which will be examined in detail in the subsequent sections.

3.3 Flow Visualization Image Sequences for High Inlet Qualities

Although the steady-state flow patterns already discussed improved our understanding on the effects of operating conditions, the flow features within the channel continuously vary with time in a periodic manner. A better understanding of this can be achieved by analyzing the high-speed image sequences portrayed in Fig. 8 for high inlet qualities. Included are image sequences for the two heat flux extremes (~10-15% and ~95% q''_{CHF}) with a time interval of 2 ms between successive images.

In Fig. 8(a), at 11.53% q''_{CHF}, focus on the high-density front just entering the channel in the first image. This HDF gradually passes through the channel and exits in the last image. The size of the HDF does not vary by much due to the very small heat flux supplied. But at 96.67% q''_{CHF}, the HDF entering the channel in the first image gradually fades away as it moves along the channel and it exits slightly sooner than at 11.53% q''_{CHF}. These both can be attributed to the higher heat flux: increased nucleate boiling within the HDF vaporizes a larger portion of liquid

and this increased vapor produces higher flow velocity in the downstream portion of the channel (note that for both heat fluxes, the inlet conditions are identical meaning the inlet velocities are equal). Figure 8(b) shows similar flow behavior except that the HDFs are thinner and lighter owing to the higher inlet quality of $x_{e,in} = 0.518$, an earlier HDF exit from the channel owing to the higher mass velocity of $G = 789.97$ kg/m^{2}s, and a weaker vaporization of the HDFs due to heat being supplied from only one wall instead of two (while the heat flux is roughly the same for both cases).

3.4 Flow Visualization Image Sequences for Low Inlet Qualities

As opposed to high inlet qualities, the periodic flow behavior at steady state is more drastic and complex for low inlet qualities. High-speed video image sequences are portrayed in Fig. 9 for a low saturated inlet quality of $x_{e,in} = 0.129$ and a low heat flux of $q''_w = 15.45\%\ q''_{CHF}$ with double-sided heating. By designating the first image to be captured at $t = 0$ ms, the time instants of other images with respect to the first image are denoted below it. The overall transient behavior can be understood from the sequence in Fig. 9(a), which covers a longer time period of $t = 600$ ms with a 20 ms time interval between successive images. Clearly two different time periods are observed: a high-density-dominant period and a low-density-dominant period. The low-density-dominant period extends from $t = 0$ until 160 ms, characterized by an overall light region interspersed with thin HDFs passing through it at regular intervals. The high-density-dominant period is seen to extend from $t = 180$ until about 360 ms, characterized by an overall darker region with some LDFs at some time instants. This cycle keeps repeating periodically. A temporally zoomed-in set of sequential images corresponding to the low-density-dominant period is shown in Fig. 9(b); these images are 2 ms apart. This sequence is similar to the image sequences for high inlet qualities shown in Fig. 8(a) at 11.53% q''_{CHF}. The transition from low-density-dominant to high-density-dominant period is shown in Fig. 9(c) as the advancement of an HDF through the channel. But unlike the short HDFs discussed previously, this HDF is much longer where the liquid occupies the entirety of the channel as seen in the latter six images. The heat transfer mechanism for LDFs is primarily the evaporation of the thin annular liquid film surrounding the central vapor core or elongated bubble (as already noted, small bubble nucleation is also observed within the LDFs' liquid film), and that for HDFs is nucleate boiling of the liquid. Thus, the heat transfer mechanism keeps alternating as per the passage of the respective fronts. The mechanism of this transience (periodically alternate passage of low- and high-density fronts) can be attributed to Density Wave Oscillations (DWO; a type of non-severe two-phase instability), which has been discussed in detail by O'Neill *et al*. [62–64] for this flow geometry. Further analysis of DWOs is beyond the scope

of the present study and the readers are directed to [62–64] which were formulated by collecting pressure signals at a sampling frequency of 200 Hz compared to the 5 Hz in this study.

High-speed video image sequences, for the same set of operating conditions and heating configuration except for a higher heat flux of 95.41% q''_{CHF}, are shown in Fig. 10. The time periods of high-density-dominant and low-density-dominant periods in Fig. 10(a) seem to be slightly different than in Fig. 9(a). But Figs. 10(b) and 10(c) are respectively similar to 9(b) and 9(c), except that the HDFs fade away as they move toward the exit due to the higher heat flux causing increased vaporization. Even very close to (and at) CHF, there are high-density-dominant periods during which liquid almost fills the entire channel. This substantiates the hypothesis that the CHF mechanism for saturated inlet is more complex and possibly related to the near-wall vapor behavior within the liquid film.

4. Heat Transfer Results and Discussion

Steady-state heat transfer results of the MST experiments with saturated inlet, in terms of flow boiling curves, local wall temperature profiles, local heat transfer coefficient profiles, and average heat transfer coefficients are presented and discussed here.

4.1 Flow Boiling Curves

Flow boiling curves are a typical way to demonstrate the heat transfer performance of two-phase thermal management schemes for various sets of operating conditions and heating configurations. In this study, boiling curves are plotted for each heated wall as the wall heat flux versus the respective average wall superheat, which is defined as the average wall temperature, $\overline{T}_w$, minus the inlet saturation temperature, $T_{sat,in}$ (which is based on the inlet pressure at each corresponding heat flux). Note that all boiling curves have a slope change at lower heat fluxes, typical of Onset of Nucleate Boiling (ONB) with subcooled inlet. Although it is inappropriate to use the term ONB here for flow boiling with a liquid-vapor mixture inlet, from flow visualization images, it can be inferred that bubble nucleation does indeed occur within the annular liquid layer on the heated walls, and the wall superheat is indicative of this near-wall heat transfer physics.

4.1.1 Flow Boiling Curves for Fixed Inlet Quality

Flow boiling curves for a fixed inlet quality of $x_{e,in}$ = 0.224 with double-sided heating configuration are presented in Fig. 11. Each boiling curve has a nucleate boiling portion, which is characterized by an almost vertical trend due to a small variation in wall superheat over a broad wall heat flux range. The upper limit of this linear trend corresponds to the point of Onset of Nucleate Boiling Degradation (ONBD) [57,65] (otherwise termed as *dryout incipience* in some

studies [66]), above which, increases in heat flux causes the curve to start deviating from its linear trend and leads up to CHF. Heat fluxes larger than q''_{ONBD} causes temporally intermittent and/or partial wall dryout, heat transfer degradation, and much higher wall temperatures.

For G = 379.97 and 650.00 kg/m^{2}s, the boiling curves for both walls almost perfectly overlap with almost the same q''_{CHF} confirming heat transfer symmetry and the slight deviations can be attributed to slight differences in heat fluxes from either wall. The lower portions of the boiling curves for both of these mass velocities coincide until the point of ONBD due to the dominant contribution of nucleate boiling and its negligible dependence on flow rate. Following ONBD, they diverge leading to CHF; both q''_{ONBD} and q''_{CHF} are higher for the higher mass velocity due to better ability of higher flow rates to replenish liquid to the heated walls and sustain nucleate boiling for larger heat fluxes. The same trends are exhibited upon increasing G to 1199.96 kg/m^{2}s, except that the nucleate boiling portion of the curves are offset to the left and the two walls are more offset from each other. This has been attributed to randomness in the heat transfer performance between the two walls by Kharangate *et al*. [42].

4.1.2 Flow Boiling Curves for Fixed Mass Velocities

Boiling curves for both single- and double-sided heating configurations at various operating conditions are respectively shown in Fig. 12(a) and 12(b). Mass velocity is maintained constant in each sub-plot. In Fig. 12(a), for G = 790.01 kg/m^{2}s and $x_{e,in} \approx 0.142$, both the wall 1 (left) and wall 2 (right) heated cases yield almost the same boiling curves, suggesting no preferential heating between the two walls and an almost mirrored flow behavior, as expected for vertical upflow. All other single-sided heating cases were conducted by heating wall 2 only. Upon increasing the inlet quality to $x_{e,in}$ = 0.518, the boiling curve starts with a similar trend at low heat fluxes and the slight offset is attributed to the ~26 kPa higher inlet pressure causing a higher $T_{sat,in}$. The curve deviates from the nucleate boiling region at a much lower heat flux and yields a much lower q''_{CHF}; both of these are a direct result of the higher amount of vapor within the channel and an increased chance of partial dryout of the liquid film along the heated walls. At G = 1599.94 kg/m^{2}s and $x_{e,in} \approx 0.033$, the curves almost overlap in spite of p_{in} being ~9 kPa different, suggesting that the effects of p_{in} are rather insignificant for small differences in it. The small difference in q''_{CHF} is within its isolation error.

In Fig. 12(b), both at G = 500.04 and 1199.95 kg/m^{2}s, the curves overlap until ONBD, which is observed at larger heat fluxes at smaller $x_{e,in}$ due to the larger amount of liquid entering the channel. However, at G = 1199.95 kg/m^{2}s, q''_{CHF} is almost equal to each other for both $x_{e,in}$ = 0.129 and 0.218 probably due to the non-monotonic trend of q''_{CHF} versus $x_{e,in}$ and these $x_{e,in}$ values being on either sides of the q''_{CHF} peak (refer to section 5.1 for more details).

Overall, both G and $x_{e,in}$ seem to play the most important role, although opposing, in determining the nature of the saturated-inlet boiling curves. p_{in} and heating configuration do affect the boiling curves, but are rather less significant.

4.2 Local Wall Temperature

Streamwise local wall temperature ($T_{w,z}$) profiles are included in Figs. 13(a) and 13(b) for different heat fluxes with single- and double-sided heating configurations, respectively, at a variety of operating conditions. Four different sets of operating conditions are assessed for each heating configuration; arranged from the top to bottom are plots for increasing $x_{e,in}$, corresponding to which are other operating conditions at different parts of their ranges. Within each plot are included $T_{w,z}$ profiles for different heat fluxes ranging from ~10% q''_{CHF} to the heat flux increment preceding CHF.

At all operating conditions, the T_w at each streamwise location monotonically increases with increasing heat flux. $T_{w,z}$ profiles at low heat fluxes are rather flat indicating an almost isothermal wall. As heat flux is increased, the profiles become symmetrically more concave downwards with T_w minima locally observed near the inlet and the exit. T_w is lowest near the inlet due to thermal entrance effects and locally being very close to the inlet fluid temperature. T_w then increases for a short distance downstream due to diminishing thermal-boundary-layer development effects. Since the flow is vertically upwards, any produced vapor further accelerates the flow due to an increase in both specific volume and buoyancy. This increased flow velocity in turn helps in more cooling of the wall due to increased turbulence and fluid mixing, and better vapor removal from the channel. At a certain location in the channel, these flow acceleration effects dominate over the effects of heat addition and T_w decreases. Flow acceleration effects are expected to be greater at higher inlet qualities and/or higher heat fluxes. The lower T_w at both ends of the heated strip could also possibly be caused by the extended heat transfer area covered by the end resistors, leading to a slightly lower local heat flux at both ends than that observed for the majority of the heated length. Based on the operating conditions, close to q''_{CHF}, the symmetry of the $T_{w,z}$ profiles is disturbed and their peaks are shifted slightly towards the exit. In Fig. 13(a), the highest-heat-flux $T_{w,z}$ profile for $x_{e,in} = 0.035$ is almost symmetrical with the maximum T_w between measurement locations 3 and 6 (refer to Fig. 2(c) for designation). As $x_{e,in}$ is increased to 0.143, the maximum T_w is observed between measurement locations 4 and 6. At high inlet qualities of $x_{e,in} = 0.430$ and 0.518, the measured maximum T_w is a sharp peak at measurement location 6, *i.e.*, a short distance upstream of the channel exit. This is directly attributed to $x_{e,in}$ which dictates vapor void fraction. When the void fraction is low, as confirmed from the high-speed images in section 3, the entire channel was temporally almost fully filled with liquid, which made the wall temperature more

uniform in the middle of the channel. But the higher void fraction experiments did not show this flow behavior, and CHF occurred sharply at a further downstream location near the exit. As confirmed in previous studies with subcooled inlet [21,22,57], CHF is not observed at the exit, but rather at these maximum T_w locations slightly upstream of the exit.

The double-sided heating cases in Fig. 13(b) overall portray similar trends as seen in Fig. 13(a) for similar $x_{e,in}$. Although a direct comparison is not possible due to differences in operating conditions between the two heating configurations, some differences would be due to the following reasons: (i) for the same heat flux, double-sided heating would double the amount of heat to the fluid, (ii) the increased heat addition would produce more vapor and lead to larger flow acceleration, and (iii) although not clearly evident in the high-speed images, possible interaction between the vapor being produced at either wall. The profiles corresponding to both walls are very similar and mostly overlap. The differences are attributed to (i) small differences in wall heat fluxes caused by electrical non-uniformity, and (ii) slightly preferential vapor production due to possibly uneven distribution of incipience cavities on either wall, even though the two copper surfaces were polished to the same finish.

4.3 Local Heat Transfer Coefficient

Streamwise local heat transfer coefficient (h_z) profiles are included in Figs. 14(a) and 14(b) for different heat fluxes with single- and double-sided heating configurations, respectively, at a variety of operating conditions. The overall layout of Fig. 14 and the operating conditions of each sub-plot are exactly the same as Fig. 13. Note that some lower heat flux percentages in Fig. 13 are omitted in Fig. 14. As already discussed in section 2.7, these lower heat fluxes yield wall temperatures very close to the local fluid saturation temperature resulting in abnormally high local heat transfer coefficient magnitudes (be it positive or negative) and sometimes even singularities; these are due to data being within the measurement uncertainties.

In Fig. 14(a), at $x_{e,in} = 0.035$, for all heat fluxes, h is highest nearest the entrance due to thermal entrance effects, then decreases appreciably for a short distance downstream until it reaches the minimum due to the flow becoming thermally fully developed, remains rather constant in the channel middle, and finally increases gradually toward the exit due to flow acceleration effects. At any streamwise location, the h_z profiles increase in magnitude until 72.21% q''_{CHF}, and higher heat fluxes close to q''_{CHF} lead to an overall reduced h_z profile due to intermittent and/or partial dryout and insulation of the heated wall with the produced vapor. These same trends are also observed at higher inlet qualities. Notice how the h_z profiles for ~95-99% q''_{CHF} are the lowest compared to those for the other heat fluxes for their operating conditions, and as $x_{e,in}$ increases, these profiles have lesser magnitudes and shift downwards. The highest heat flux of 94.12% q''_{CHF}

in the top-most plot does convey degraded heat transfer, which is not very severe to bring the entire h_z profile to the bottom.

Overall, the double-sided heating cases in Fig. 14(b) yield similar trends as single-sided heating. The differences in the h_z profiles between the two heating configurations and between each wall during double-sided heating can be explained by the same reasons discussed in section 4.2.

4.4 Average Heat Transfer Coefficient

Average heat transfer coefficient ($\bar{h}$) variations with wall heat flux are included in Figs. 15(a), 15(b), and 15(c), respectively for single-sided heating at fixed G, double-sided heating at fixed G, and double-sided heating at fixed $x_{e,in}$. Included in each plot are curves for different operating parameters. It is again noted that, as already reasoned in sections 2.7 and 4.3, some of the lowest heat flux datapoints are excluded. All curves follow the same trend: a very high heat transfer coefficient at very low heat fluxes due to the wall temperature being very close to the fluid temperature, a sharp decrease as heat flux is increased until a local minimum, followed by a gradual increase leading to a local maximum, and finally another decrease at high heat fluxes leading to a minimum at CHF. It is hypothesized that the very high $\bar{h}$ at very low heat fluxes is due to the large contribution of bubble nuleation within the annular liquid layer to cooling the wall, and the extreme $\bar{h}$ decline with increasing heat flux is due to be the much reduced contribution of nucleation boiling heat transfer and transition to convective boiling dominant heat transfer. The gradual increase is due to the dominance of convective boiling heat transfer and moderate heat fluxes producing more vapor causing larger flow acceleration. At the peak, the positively-impacting acceleration effects are matched by the negatively-impacting larger void fraction within the channel. The decrease downstream of the peak is due to the much larger vapor void within the channel preventing sufficient fresh liquid replenishment to the heated walls, resulting in temporal and/or partial dryout.

In Fig. 15(a), for G = 790.01 kg/m^{2}s, $x_{e,in}$ = 0.518 yields a higher $\bar{h}$ than that for 0.140 at lower heat fluxes and lower $\bar{h}$ at higher heat fluxes. For the same G, higher $x_{e,in}$ means a higher liquid-vapor mixture velocity through the channel due to flow acceleration and a higher vapor void fraction. At higher $x_{e,in}$, these effects lead to a fast-moving thin film along the heated wall yielding higher $\bar{h}$, but at higher heat fluxes, the scarcity of liquid in the same film leads to partial dryout yeilding smaller q''_{CHF}. In Fig. 15(b), for G = 500.04 kg/m^{2}s, even though the $x_{e,in}$ increase from 0.330 to 0.401 is smaller, the same trends are observed at higher heat fluxes for the same reasons, but the difference in $\bar{h}$ is indistinct at lower heat fluxes, possibily due to the higher p_{in} and the associated difference in thermophysical properties. For G = 1199.95 kg/m^{2}s, the trends at lower

heat fluxes are the same as already explained, but there does not seem to be a clear difference in $\bar{h}$ at higher heat fluxes due to the smaller inlet qualities.

In Fig. 15(c), for the same inlet quality, higher G yields both a higher q''_{CHF} and a higher $\bar{h}$ both at lower and higher heat fluxes due to the increased mixing of the two-phase mixture, increased turbulence, and ability to remove the produced vapor along the heated wall and replenish it with liquid for both evaporation and nucleate boiling.

5. Experimental CHF Results and Model Predictions

5.1 Consolidated CHF Database and Experimental Trends

Leading up to the experiments on the ISS, a consolidated CHF database for saturated two-phase inlet was compiled from CHF data obtained both during the MST as well as some prior experiments [48,54]. This creates a comprehensive database consisting of a vast range of operating conditions, heating configurations, and flow orientations with respect to Earth gravity. A summary of the operating parameter ranges of the consolidated saturated-inlet CHF database is provided in Table 4.

Experimental results of a sample of the CHF database are shown in Fig. 16. Figs. 16(a) and 16(b) show CHF results for two different ranges of inlet quality at different orientations and mass velocities for single- and double-sided heating, respectively. Similar trends exist between the two heating configurations. q''_{CHF} is shown to be strongly a function of mass velocity. For both configurations, increasing the mass velocity has shown to increase q''_{CHF} for all orientations. One exception is for horizontal single-sided bottom heating, increasing the mass velocity from $G \approx 200$ to 400 kg/m^{2}s yielded identical q''_{CHF} at the lower inlet quality range. q''_{CHF} at these low flow rates is expected to be similar. As observed in [54], mass velocities of $G \leq 400$ kg/m^{2}s during horizontal bottom wall heating experienced q''_{CHF} resembling pool boiling. This is also reflected at the higher inlet quality range where the increase in q''_{CHF} observed for horizontal bottom wall heating is drastically lower than other orientations when increasing mass velocity from $G \approx 200$ to 400 kg/m^{2}s. It is noted that the q''_{CHF} values being exactly identical at the lower inlet quality is due to CHF isolation error and the true q''_{CHF} would be expected to be slightly lower at $G \approx 200$ as compared to 400 kg/m^{2}s.

Focusing on single-sided heating in Fig 16(a), clear trends can be seen with respect to orientation. For both inlet quality ranges, at low mass velocities, horizontal bottom wall heating and top wall heating produced the highest and lowest q''_{CHF}, respectively. This is due to buoyancy playing a major role, causing the flow to stratify as vapor congregates along the top wall. During bottom wall heating buoyancy aides in removing vapor from the heated wall as boiling occurs and promotes liquid replenishment to the heated wall. But during horizontal top wall heating,

buoyancy has the opposite effect and creates a vapor barrier adjacent to the heated wall that prevents liquid contact, yielding low q''_{CHF}. The vertical orientations fall between horizontal top and bottom wall heating for low and intermediate flow rates with vertical upflow slightly outperforming downflow due to influence of buoyancy. In vertical upflow, buoyancy is in the same direction as flow and helps convecting the produced vapor out of the channel, but in vertical downflow, buoyancy acts against the flow and impedes the vapor from leaving the channel eventually causing CHF; but this impedance is not so severe to prevent fresh liquid replenishment to the heated wall and the respective q''_{CHF} values are larger than for horizontal top wall heating. As flow rate is increased, the influence of gravity is mitigated by the greater flow inertia and q''_{CHF} for all orientations begin to converge. This convergence occurs at a lower flow rate for higher inlet qualities due to the higher velocity of each phase and thus greater inertia. Beyond a certain G to limit orientation effects, the two $x_{e,in}$ ranges show negligible differences in q''_{CHF}.

The double-sided heating results in Fig. 16(b) portray similar trends as single-sided heating. The impact of orientation is apparent at low flow rates, and horizontal flows yield the lowest q''_{CHF} amongst all due to vapor stratification at the top heated wall. Both vertical flow orientations demonstrate negligible preference of CHF manifesting at either wall, with vertical upflow yielding the highest q''_{CHF} and downflow intermediary values between upflow and horizontal flow. Gravity independence is again achieved above a certain G, and this conclusion has already led to criteria for achieving the same for both flow boiling and condensation [51,67]. The one main difference between single- and double-sided heating is that the latter generates more vapor than the former, resulting in larger flow acceleration and gravity independence achieved at relatively lower G.

Figures 16(c) and 16(d) show the variation of q''_{CHF} with $x_{e,in}$ for $G \sim 800$ kg/m^{2}s at different orientations for single- and double-sided heating, respectively. For both heating configurations, an inconsistent trend is initially seen across the different orientations. In most cases, q''_{CHF} initially increases as $x_{e,in}$ is increased until a certain $x_{e,in}$. However, all cases show q''_{CHF} eventually decreasing with $x_{e,in}$. It can be deduced that, for a given set of operating conditions, there exists an inlet quality at which q''_{CHF} peaks and after which, q''_{CHF} decreases with quality. As $x_{e,in}$ is increased, two phenomena occur: (i) the inertia of each phase increases and (ii) the vapor void fraction within the channel increases. The former phenomenon dominates over the latter at lower $x_{e,in}$ and the latter dominates at higher $x_{e,in}$, with the crossover occurring at the $x_{e,in}$ for which the peak q''_{CHF} is observed.

5.2 CHF Model

The *Interfacial Lift-off Model*, originally developed by Galloway and Mudawar [68,69], has shown excellent accuracy in predicting flow boiling CHF for a variety of inlet conditions, heating configurations, and gravitational environments [22,41,58]. The model describes a wavy vapor layer that forms along the heated wall. Troughs in the wavy interface between the liquid and vapor, called *wetting fronts*, allow for liquid to access the heated wall. Within the wetting fronts, vigorous boiling occurs as they propagate down the heated wall. Wetting fronts are hypothesized to be the last source of cooling for the heated wall, and CHF is postulated to occur when vapor momentum at the wetting front causes it to lift off the heated wall. At this point, boiling is halted and the heat that was being removed in the now detached wetting front is transferred axially to neighboring wetting fronts causing a chain reaction of wetting front extinguishment. Kharangate *et al*. [48] showed the model can be modified to accurately predict CHF for two-phase inlet conditions. This version of the *Interfacial Lift-off Model* is used here to make CHF predictions for the consolidated saturated-inlet FBCE-CHF database. A brief description of the model and its procedure are provided for a case with single-sided heating. A summary of key equations required in the model are provided in Table 5; note that $g = g_e$ for this study because the entire database was obtained in Earth gravity. Further details of the model and description for double-sided heating can be found in [48].

The Interfacial Lift-off Model is composed of 4 sub-models that are used in conjunction to predict CHF. First, a separated flow model is used to predict axial variations in pressure, phase velocities, quality, and void fraction. The modeled cross-section of the flow for single-sided heating with inlet void is shown in Fig. 17, where each layer is assumed to be its own phase. For the example depicted, three phases are utilized: the central vapor core, annular liquid layer of uniform thickness ε, and vapor layer generated along the heated wall. Note that for a case with double-sided heating, another vapor layer would be present along the other heated wall. These parameters will be used as inputs for the remaining sub-models. It is important to note the following assumptions adopted for the separated flow model:

(i) the vapor layer along the wall is initiated at the leading edge of the heated wall,

(ii) the vapor core maintains its quality along the channel,

(iii) velocity of each phase layer is uniform within the channel's cross-section,

(iv) pressure is uniform across the channel's entire cross-section,

(v) phases are maintained at local saturation temperature,

(vi) vapor produced at the wetting front does not contribute to streamwise momentum, and,

(vii) during double-sided heating, equal heat flux is applied to each heated wall.

The next sub-model to be applied is based on classical instability theory [69–71] of two fluids moving at different velocities and is utilized to describe the interface between the liquid

layer and vapor layer along the heated wall as an ideal sinusoid. The stability of the interface is determined by the relative magnitudes of inertia, surface tension, and body force. The goals of the stability analysis are to determine the critical wavelength of the interface, which corresponds to the onset of instability, and the interfacial curvature and its associated pressure force which holds wetting fronts against the heated wall.

The final two sub-models are used to calculate the heat flux required to initiate lift-off. CHF is triggered once the momentum of vapor normal to the wall in the wetting front exceeds the pressure force associated with interfacial curvature. A simple energy balance is then used to relate the wall heat flux to the heat flux concentrated in the wetting fronts.

The model is initiated by determining the channel's inlet void fraction by utilizing the conservation of momentum equations of the separated flow model with adiabatic conditions. The channel is assumed to contain a vapor core with liquid surrounding it as depicted in Fig. 17. q''_{CHF} is then predicted, and the separated flow model is called upon coupled with a fourth-order Runga-Kutta numerical scheme to determine the flow properties along the channel. During solution of the separated flow model, the axial location where the velocity of the vapor phase surpasses that of the liquid phase is recorded as z_o. A critical wavelength, λ_c, is assumed and the separated flow model is proceeded with until z^*, where $z^* = z_o + \lambda_c$. A new critical wavelength is determined using the equation in Table 5 and this process is repeated until the assumed wavelength equals the calculated wavelength. Once the critical wavelength for the assumed heat flux is known, q''_{CHF} is found using the equation provided in Table 5, evaluated at z^*. The entire process is repeated until the assumed heat flux converges to the calculated q''_{CHF}. In the case of double-sided heating, the process is repeated for each heated wall and the minimum of the q''_{CHF} values obtained for each wall is deemed the true q''_{CHF}.

5.3 Comparison of CHF Model Predictions with Experimental Data

While the Interfacial Lift-off model has proven to be effective for a broad range of operating conditions, limitations exist for the applicability of the model. Kharangate *et al.* [48] observed that the interfacial behavior was entirely dominated by the effects of gravity for $G \leq 400$ kg/m^{2}s. In the present study, the *Interfacial Lift-off Model* is utilized to predict q''_{CHF} for all cases with $G \geq 500$ kg/m^{2}s, which is slightly higher than the visual evidence suggests in order to limit errors occurring at transition from the gravity dominated regime. The finalized set of operating conditions tasked to the Interfacial Lift-off model is presented in Table 6. Figs. 18(a) and 18(b) compare q''_{CHF} predicted by the *Interfacial Lift-off Model* to experimental q''_{CHF} for a subset of the consolidated database described in Table 6 for single- and double-sided heating, respectively. The

predictive accuracy of each model is determined by calculating the mean absolute error, *MAE*, and statistical inliers, ξ_{15} and ξ_{30}. With N data points, the *MAE* is calculated as

$$MAE(\%) = \frac{1}{N}\sum\left|\frac{q''_{CHF,pred} - q''_{CHF,exp}}{q''_{CHF,exp}}\right| \times 100 . \quad (9)$$

Figure 18(a) shows q''_{CHF} for single-sided heating is predicted with a *MAE* of 10.16% (for N = 66) with 95.45% of datapoints predicted within ±30%. Fig. 18(b) shows a *MAE* of 14.27% (for N = 52) for double-sided heating with 86.54% of datapoints predicted within ±30%. These statistics reflect excellent predictive capability for both heating configurations and a wide range of operating conditions. Further details regarding the predictive capabilities of the *Interfacial Lift-off Model* at each orientation are available in Table 6.

6. Conclusions

This study explored flow boiling of nPFH with saturated mixture inlet based on results obtained from the final pre-launch Earth-gravity Mission Sequence Tests (MST) of the Flow Boiling and Condensation Experiment's (FBCE) Flow Boiling Module (FBM) in vertically upflow orientation. Experiments were performed using the same experimental system that was launched to the International Space Station (ISS) in August 2021. High-speed video photographs were presented for various operating conditions and assessed. Heat transfer results in terms of flow boiling curves, streamwise wall temperature profiles, streamwise heat transfer coefficient profiles, and average heat transfer coefficients were presented and explained. In order to broaden the scope of analysis with broader ranges of operating conditions and different orientations, CHF data from the MST were combined with some prior databases to form a consolidated FBCE-CHF database for saturated inlet. CHF trends from this database were explained and the interfacial lift-off model employed to make predictions. Key conclusions from this study are:

(1) The high-speed images for saturated inlet were not as clear or distinct as those for subcooled inlet. Density wave oscillations were prominent with low- and high-density fronts passing through the channel, the lengths of which were dependent on the operating conditions. The flow patterns within the heated section were mainly dictated by the inlet quality. High inlet qualities showed a predominantly vapor-filled channel interspersed with thin high-density fronts. Low inlet qualities displayed a more complex periodic behavior with alternating high-density-dominant and low-density-dominant periods. The low-density-dominant period was similar to high inlet qualities while the high-density-dominant period had very long high-density fronts filling up the entirety of the channel with mostly liquid. No discernible differences were seen upon increasing the heat flux from a minimum until CHF. Careful examination showed small bubbles nucleating within the liquid film next to the wall.

(2) Inlet quality and mass velocity played the most important role in determining the flow boiling curves. Lower inlet qualities and/or higher mass velocities yielded better heat transfer performances and higher q''_{CHF}.

(3) Both the streamwise wall temperature and heat transfer coefficient profiles showed CHF to manifest not at the exit, but rather a short distance upstream of the exit.

(4) Upon increasing wall heat flux, average heat transfer coefficient decreased from very high values, reached a local minimum, gradually increased until a local maximum, and finally decreased again to a minimum at CHF.

(5) The consolidated FBCE-CHF database showed, for single-sided heating, q''_{CHF} to be higher in the order of horizontal flow bottom wall heated, vertical upflow, vertical downflow, and horizontal flow top wall heated. Gravity independence was achieved at higher mass velocities. Increasing mass velocity monotonically increased q''_{CHF}, but increasing inlet quality led q''_{CHF} to first increase until a peak and then decrease.

(6) The interfacial lift-off model showed good accuracy in predicting CHF values with an overall mean absolute error of 11.97% for the consolidated FBCE-CHF database constrained by mass velocities ≥ 500 kg/m^{2}s.

(7) Overall, MST of the FBCE's FBM was successful for saturated inlet conditions. The ISS-destined experimental facility worked as intended and some minor unexpected snags during MST can be easily addressed with minor tweaks to the future operating procedure. Further analysis of all data confirmed reliability of the upcoming ISS data.

Declaration of Competing Interest – None. The authors declare that they have no known competing financial interests or personal relationships that could have appeared to influence the work reported in this paper.

Acknowledgement – The authors are appreciative of the support of the National Aeronautics and Space Administration (NASA) under grant no. NNX17AK98G. The authors are also thankful to the FBCE personnel at NASA Glenn Research Center, Cleveland, Ohio, especially Nancy Hall (FBCE Project Manager), Rochelle May and Phillip Gonia (Software Engineering), Mark Sorrells (Assembly, Integration and Test Lead), Jesse DeFiebre (Fluids Lead), Monica Guzik (FBCE Chief Engineer), and ZIN FCF Mission Operations Team, for their dedicated technical assistance and successful completion of the MST. This work was also partly supported by Purdue University's Bilsland Dissertation Fellowship.

References

[1] T.J. LaClair, I. Mudawar, Thermal transients in a capillary evaporator prior to the initiation of boiling, Int. J. Heat Mass Transfer 43 (21) (2000) 3937–3952, doi: 10.1016/S0017-9310(00)00042-

9.

[2] I. Mudawar, R.A. Houpt, Mass and momentum transport in smooth falling liquid films laminarized at relatively high Reynolds numbers, Int. J. Heat Mass Transfer 36 (14) (1993) 3437–3448, doi: 10.1016/0017-9310(93)90162-Y.

[3] C.O. Gersey, I. Mudawar, Effects of heater length and orientation on the trigger mechanism for near-saturated flow boiling critical heat flux—I. Photographic study and statistical characterization of the near-wall interfacial features, Int. J. Heat Mass Transfer 38 (4) (1995) 629–641, doi: 10.1016/0017-9310(94)00193-Y.

[4] C.O. Gersey, I. Mudawar, Effects of heater length and orientation on the trigger mechanism for near-saturated flow boiling critical heat flux-II. Critical heat flux model, Int. J. Heat Mass Transfer 38 (4) (1995) 643–654, doi: 10.1016/0017-9310(94)00194-Z.

[5] V.S. Devahdhanush, Y. Lei, Z. Chen, I. Mudawar, Assessing advantages and disadvantages of macro- and micro-channel flow boiling for high-heat-flux thermal management using computational and theoretical/empirical methods, Int. J. Heat Mass Transfer 169 (2021) 120787, doi: 10.1016/j.ijheatmasstransfer.2020.120787.

[6] G. Liang, I. Mudawar, Review of single-phase and two-phase nanofluid heat transfer in macro-channels and micro-channels, Int. J. Heat Mass Transfer 136 (2019) 324–354, doi: 10.1016/j.ijheatmasstransfer.2019.02.086.

[7] S. Mukherjee, I. Mudawar, Pumpless loop for narrow channel and micro-channel boiling, J. Electron. Packag. 125 (3) (2003) 431–441, doi: 10.1115/1.1602708.

[8] V.S. Devahdhanush, S. Lee, I. Mudawar, Experimental investigation of subcooled flow boiling in annuli with reference to thermal management of ultra-fast electric vehicle charging cables, Int. J. Heat Mass Transfer 172 (2021) 121176, doi: 10.1016/j.ijheatmasstransfer.2021.121176.

[9] I. Mudawar, T.M. Anderson, Parametric investigation into the effects of pressure, subcooling, surface augmentation and choice of coolant on pool boiling in the design of cooling systems for high-power-density electronic chips, J. Electron. Packag. 112 (4) (1990) 375–382, doi: 10.1115/1.2904392.

[10] G. Liang, I. Mudawar, Review of pool boiling enhancement with additives and nanofluids, Int. J. Heat Mass Transfer 124 (2018) 423–453, doi: 10.1016/j.ijheatmasstransfer.2018.03.046.

[11] M.E. Johns, I. Mudawar, An ultra-high power two-phase jet-impingement avionic clamshell module, J. Electron. Packag. 118 (4) (1996) 264–270, doi: 10.1115/1.2792162.

[12] V.S. Devahdhanush, I. Mudawar, Review of critical heat flux (CHF) in jet impingement boiling, Int. J. Heat Mass Transfer 169 (2021) 120893, doi: 10.1016/j.ijheatmasstransfer.2020.120893.

[13] M. Visaria, I. Mudawar, Application of two-phase spray cooling for thermal management of electronic devices, IEEE Trans. Compon. Packag. Technol. 32 (4) (2009) 784–793, doi: 10.1109/TCAPT.2008.2010405.

[14] M.K. Sung, I. Mudawar, Effects of jet pattern on two-phase performance of hybrid micro-channel/micro-circular-jet-impingement thermal management scheme, Int. J. Heat Mass Transfer 52 (13–14) (2009) 3364–3372, doi: 10.1016/j.ijheatmasstransfer.2008.06.046.

[15] M.K. Sung, I. Mudawar, Single-phase and two-phase heat transfer characteristics of low temperature hybrid micro-channel/micro-jet impingement cooling module, Int. J. Heat Mass Transfer 51 (15–16) (2008) 3882–3895, doi: 10.1016/j.ijheatmasstransfer.2007.12.016.

[16] F.P. Chiaramonte, J.A. Joshi, Workshop on critical issues in microgravity fluids, transport, and reaction processes in advanced human support technology—Final report, TM-2004-212940, NASA,

Washington, DC, USA, 2004.

[17] National Research Council, Recapturing a Future for Space Exploration, The National Academies Press, Washington, DC, USA, 2011, doi: 10.17226/13048.

[18] C. Konishi, I. Mudawar, M.M. Hasan, Investigation of localized dryout versus CHF in saturated flow boiling, Int. J. Heat Mass Transfer 67 (2013) 131–146, doi: 10.1016/j.ijheatmasstransfer.2013.07.082.

[19] Y.F. Xue, J.F. Zhao, J.J. Wei, J. Li, D. Guo, S.X. Wan, Experimental study of nucleate pool boiling of FC-72 on smooth surface under microgravity, Microgravity Sci. Technol. 23 (2011) 75–85, doi: 10.1007/s12217-011-9274-5.

[20] M. Misawa, An experimental and analytical investigation of flow boiling heat transfer under microgravity conditions, Ph.D. thesis, University of Florida, FL, USA, 1993.

[21] C. Konishi, H. Lee, I. Mudawar, M.M. Hasan, H.K. Nahra, N.R. Hall, J.D. Wagner, R.L. May, J.R. Mackey, Flow boiling in microgravity: Part 1 – Interfacial behavior and experimental heat transfer results, Int. J. Heat Mass Transfer 81 (2015) 705–720, doi: 10.1016/j.ijheatmasstransfer.2014.10.049.

[22] C. Konishi, H. Lee, I. Mudawar, M.M. Hasan, H.K. Nahra, N.R. Hall, J.D. Wagner, R.L. May, J.R. Mackey, Flow boiling in microgravity: Part 2 – Critical heat flux interfacial behavior, experimental data, and model, Int. J. Heat Mass Transfer 81 (2015) 721–736, doi: 10.1016/j.ijheatmasstransfer.2014.10.052.

[23] T. Oka, Y. Abe, Y.H. Mori, A. Nagashima, Pool boiling of n-pentane, CFC-113, and water under reduced gravity: Parabolic flight experiments with a transparent heater, J. Heat Transfer 117 (2) (1995) 408–417, doi: 10.1115/1.2822537.

[24] J. Kim, J.F. Benton, D. Wisniewski, Pool boiling heat transfer on small heaters: Effect of gravity and subcooling, Int. J. Heat Mass Transfer 45 (19) (2002) 3919–3932, doi: 10.1016/S0017-9310(02)00108-4.

[25] A. Weinzierl, J. Straub, Nucleate pool boiling in microgravity environment, in: Proc. Int. Heat Transfer Conf. 7, Begell House Inc., Munich, Germany, 1982, pp. 21–27, doi: 10.1615/IHTC7.3730.

[26] V.K. Dhir, G.R. Warrier, E. Aktinol, D. Chao, J. Eggers, W. Sheredy, W. Booth, Nucleate pool boiling experiments (NPBX) on the International Space Station, Microgravity Sci. Technol. 24 (5) (2012) 307–325, doi: 10.1007/s12217-012-9315-8.

[27] J. Straub, Boiling heat transfer and bubble dynamics in microgravity, Adv. Heat Transfer 35 (2001) 57–172, doi: 10.1016/S0065-2717(01)80020-4.

[28] H. Merte, Momentum effects in steady nucleate pool boiling during microgravity, Ann. N. Y. Acad. Sci. 1027 (2004) 196–216, doi: 10.1196/annals.1324.018.

[29] C. Colin, J. Fabre, A.E. Dukler, Gas-liquid flow at microgravity conditions—I. Dispersed bubble and slug flow, Int. J. Multiphase Flow 17 (4) (1991) 533–544, doi: 10.1016/0301-9322(91)90048-8.

[30] A.E. Dukler, J.A. Fabre, J.B. McQuillen, R. Vernon, Gas-liquid flow at microgravity conditions: Flow patterns and their transitions, Int. J. Multiphase Flow 14 (4) (1988) 389–400, doi: 10.1016/0301-9322(88)90017-1.

[31] M. Saito, N. Yamaoka, K. Miyazaki, M. Kinoshita, Y. Abe, Boiling two-phase flow under microgravity, Nucl. Eng. Des. 146 (1–3) (1994) 451–461, doi: 10.1016/0029-5493(94)90350-6.

[32] H. Ohta, Experiments on microgravity boiling heat transfer by using transparent heaters, Nucl. Eng. Des. 175 (1–2) (1997) 167–180, doi: 10.1016/S0029-5493(97)00172-6.

[33] C. Baltis, G.P. Celata, M. Cumo, L. Saraceno, G. Zummo, Gravity influence on heat transfer rate in flow boiling, Microgravity Sci. Technol. 24 (3) (2012) 203–213, doi: 10.1007/s12217-012-9298-5.

[34] S. Luciani, D. Brutin, C. Le Niliot, O. Rahli, L. Tadrist, Flow boiling in minichannels under normal, hyper-, and microgravity: Local heat transfer analysis using inverse methods, J. Heat Transfer 130 (10) (2008) 1–13, doi: 10.1115/1.2953306.

[35] S. Luciani, D. Brutin, C. Le Niliot, L. Tadrist, O. Rahli, Boiling heat transfer in a vertical microchannel: Local estimation during flow boiling with a non intrusive method, Multiphase Sci. Technol. 21 (4) (2009) 297–328, doi: 10.1615/MultScienTechn.v21.i4.30.

[36] H. Ohta, H. Asano, O. Kawanami, K. Suzuki, R. Imai, Y. Shinmoto, S. Matsumoto, T. Kurimoto, H. Takaoka, K. Fujii, M. Sakamoto, K. Sawada, H. Kawasaki, A. Okamoto, K. Kogure, T. Oka, K. Usuku, T. Tomobe, M. Takayanagi, Development of boiling and two-phase flow experiments on board ISS (Research objectives and concept of experimental setup), Int. J. Microgravity Sci. Appl. 33 (1) (2016) 330101, doi: 10.15011/ijmsa.33.330102.

[37] K. Inoue, H. Ohta, Y. Toyoshima, H. Asano, O. Kawanami, R. Imai, K. Suzuki, Y. Shinmoto, S. Matsumoto, Heat loss analysis of flow boiling experiments onboard International Space Station with unclear thermal environmental conditions (1st Report: Subcooled liquid flow conditions at test section inlet), Microgravity Sci. Technol. 33 (2) (2021) 28, doi: 10.1007/s12217-021-09869-5.

[38] K. Inoue, H. Ohta, H. Asano, O. Kawanami, R. Imai, K. Suzuki, Y. Shinmoto, T. Kurimoto, S. Matsumoto, Heat loss analysis of flow boiling experiments onboard International Space Station with unclear thermal environmental conditions (2nd Report: Liquid-vapor two-phase flow conditions at test section inlet), Microgravity Sci. Technol. 33 (5) (2021) 57, doi: 10.1007/s12217-021-09902-7.

[39] C. Konishi, I. Mudawar, M.M. Hasan, Investigation of the influence of orientation on critical heat flux for flow boiling with two-phase inlet, Int. J. Heat Mass Transfer 61 (2013) 176–190, doi: 10.1016/j.ijheatmasstransfer.2013.01.076.

[40] H. Zhang, I. Mudawar, M.M. Hasan, Experimental and theoretical study of orientation effects on flow boiling CHF, Int. J. Heat Mass Transfer 45 (22) (2002) 4463–4477, doi: 10.1016/S0017-9310(02)00152-7.

[41] H. Zhang, I. Mudawar, M.M. Hasan, CHF model for subcooled flow boiling in Earth gravity and microgravity, Int. J. Heat Mass Transfer 50 (19–20) (2007) 4039–4051, doi: 10.1016/j.ijheatmasstransfer.2007.01.029.

[42] C.R. Kharangate, L.E. O'Neill, I. Mudawar, L.E. O'Neill, I. Mudawar, L.E. O'Neill, I. Mudawar, Effects of two-phase inlet quality, mass velocity, flow orientation, and heating perimeter on flow boiling in a rectangular channel: Part 1 – Two-phase flow and heat transfer results, Int. J. Heat Mass Transfer 103 (2016) 1261–1279, doi: 10.1016/j.ijheatmasstransfer.2016.05.060.

[43] C.L. Ong, Macro-to-microchannel transition in two-phase flow and evaporation, Ph.D. Thesis, École Polytechnique Fédérale de Lausanne, Switzerland, 2010, doi: 10.5075/epfl-thesis-4674.

[44] W. Qu, I. Mudawar, Measurement and correlation of critical heat flux in two-phase micro-channel heat sinks, Int. J. Heat Mass Transfer 47 (10–11) (2004) 2045–2059, doi: 10.1016/j.ijheatmasstransfer.2003.12.006.

[45] B. Agostini, R. Revellin, J.R. Thome, M. Fabbri, B. Michel, D. Calmi, U. Kloter, High heat flux flow boiling in silicon multi-microchannels – Part III: Saturated critical heat flux of R236fa and two-phase pressure drops, Int. J. Heat Mass Transfer 51 (21–22) (2008) 5426–5442, doi: 10.1016/j.ijheatmasstransfer.2008.03.005.

[46] A.W. Mauro, J.R. Thome, D. Toto, G.P. Vanoli, Saturated critical heat flux in a multi-microchannel heat sink fed by a split flow system, Exp. Therm. Fluid Sci. 34 (1) (2010) 81–92, doi: 10.1016/j.expthermflusci.2009.09.005.

[47] J.E. Park, J.R. Thome, Critical heat flux in multi-microchannel copper elements with low pressure refrigerants, Int. J. Heat Mass Transfer 53 (1–3) (2010) 110–122, doi: 10.1016/j.ijheatmasstransfer.2009.09.047.

[48] C.R. Kharangate, L.E. O'Neill, I. Mudawar, Effects of two-phase inlet quality, mass velocity, flow orientation, and heating perimeter on flow boiling in a rectangular channel: Part 2 – CHF experimental results and model, Int. J. Heat Mass Transfer 103 (2016) 1280–1296, doi: 10.1016/j.ijheatmasstransfer.2016.05.059.

[49] C.B. Tibiriçá, L.E. Czelusniak, G. Ribatski, Critical heat flux in a 0.38 mm microchannel and actions for suppression of flow boiling instabilities, Exp. Therm. Fluid Sci. 67 (2015) 48–56, doi: 10.1016/j.expthermflusci.2015.02.020.

[50] T. Ueda, S. Tsunenari, M. Koyanagi, An investigation of critical heat flux and surface rewet in flow boiling systems, Int. J. Heat Mass Transfer 26 (8) (1983) 1189–1198, doi: 10.1016/S0017-9310(83)80173-2.

[51] C. Konishi, I. Mudawar, M.M. Hasan, Criteria for negating the influence of gravity on flow boiling critical heat flux with two-phase inlet conditions, Int. J. Heat Mass Transfer 65 (2013) 203–218, doi: 10.1016/j.ijheatmasstransfer.2013.05.070.

[52] C.R. Kharangate, L.E. O'Neill, I. Mudawar, M.M. Hasan, H.K. Nahra, R. Balasubramaniam, N.R. Hall, A.M. Macner, J.R. Mackey, Flow boiling and critical heat flux in horizontal channel with one-sided and double-sided heating, Int. J. Heat Mass Transfer 90 (2015) 323–338, doi: 10.1016/j.ijheatmasstransfer.2015.06.073.

[53] C.R. Kharangate, I. Mudawar, M.M. Hasan, Experimental and theoretical study of critical heat flux in vertical upflow with inlet vapor void, Int. J. Heat Mass Transfer 55 (1–3) (2012) 360–374, doi: 10.1016/j.ijheatmasstransfer.2011.09.028.

[54] C.R. Kharangate, L.E. O'Neill, I. Mudawar, M.M. Hasan, H.K. Nahra, R. Balasubramaniam, N.R. Hall, A.M. Macner, J.R. Mackey, Effects of subcooling and two-phase inlet on flow boiling heat transfer and critical heat flux in a horizontal channel with one-sided and double-sided heating, Int. J. Heat Mass Transfer 91 (2015) 1187–1205, doi: 10.1016/j.ijheatmasstransfer.2015.08.059.

[55] H. Zhang, I. Mudawar, M.M. Hasan, Flow boiling CHF in microgravity, Int. J. Heat Mass Transfer 48 (15) (2005) 3107–3118, doi: 10.1016/j.ijheatmasstransfer.2005.02.015.

[56] H.K. Nahra, M.M. Hasan, M. Guzik, R. Balasubramaniam, J.R. Mackey, Flow boiling and condensation experiment (FBCE): Capabilities and system description, NASA/TM-20205007641, NASA Glenn Research Center, Cleveland, OH, USA, 2020.

[57] V.S. Devahdhanush, I. Mudawar, H.K. Nahra, R. Balasubramaniam, M.M. Hasan, J.R. Mackey, Experimental heat transfer results and flow visualization of vertical upflow boiling in Earth gravity with subcooled inlet conditions – In preparation for experiments onboard the International Space Station, Int. J. Heat Mass Transfer 188 (2022) 122603, doi: 10.1016/j.ijheatmasstransfer.2022.122603.

[58] S.J. Darges, V.S. Devahdhanush, I. Mudawar, H.K. Nahra, R. Balasubramaniam, M.M. Hasan, J.R. Mackey, Experimental results and interfacial lift-off model predictions of critical heat flux for flow boiling with subcooled inlet conditions – In preparation for experiments onboard the International Space Station, Int. J. Heat Mass Transfer 183 (2022) 122241, doi: 10.1016/j.ijheatmasstransfer.2021.122241.

[59] S. Lee, V.S. Devahdhanush, I. Mudawar, Experimental and analytical investigation of flow loop induced instabilities in micro-channel heat sinks, Int. J. Heat Mass Transfer 140 (2019) 303–330, doi: 10.1016/j.ijheatmasstransfer.2019.05.077.

[60] L.E. O'Neill, I. Mudawar, Review of two-phase flow instabilities in macro- and micro-channel

systems, Int. J. Heat Mass Transfer 157 (2020) 119738, doi: 10.1016/j.ijheatmasstransfer.2020.119738.

[61] E.W. Lemmon, I.H. Bell, M.L. Huber, M.O. McLinden, NIST Standard Reference Database 23: Reference Fluid Thermodynamic and Transport Properties-REFPROP, Version 10, NIST, Gaithersburg, MD, USA, 2018.

[62] L.E. O'Neill, I. Mudawar, M.M. Hasan, H.K. Nahra, R. Balasubramaniam, N.R. Hall, A. Lokey, J.R. Mackey, Experimental investigation into the impact of density wave oscillations on flow boiling system dynamic behavior and stability, Int. J. Heat Mass Transfer 120 (2018) 144–166, doi: 10.1016/j.ijheatmasstransfer.2017.12.011.

[63] L.E. O'Neill, I. Mudawar, M.M. Hasan, H.K. Nahra, R. Balasubramaniam, J.R. Mackey, Experimental investigation of frequency and amplitude of density wave oscillations in vertical upflow boiling, Int. J. Heat Mass Transfer 125 (2018) 1240–1263, doi: 10.1016/j.ijheatmasstransfer.2018.04.138.

[64] L.E. O'Neill, I. Mudawar, Mechanistic model to predict frequency and amplitude of Density Wave Oscillations in vertical upflow boiling, Int. J. Heat Mass Transfer 123 (2018) 143–171, doi: 10.1016/j.ijheatmasstransfer.2018.02.078.

[65] V.S. Devahdhanush, I. Mudawar, Critical heat flux of confined round single jet and jet array impingement boiling, Int. J. Heat Mass Transfer 169 (2021) 120857, doi: 10.1016/j.ijheatmasstransfer.2020.120857.

[66] S.M. Kim, I. Mudawar, Universal approach to predicting saturated flow boiling heat transfer in mini/micro-channels – Part I. Dryout incipience quality, Int. J. Heat Mass Transfer 64 (2013) 1226–1238, doi: 10.1016/j.ijheatmasstransfer.2013.04.016.

[67] L.E. O'Neill, I. Park, C.R. Kharangate, V.S. Devahdhanush, V. Ganesan, I. Mudawar, Assessment of body force effects in flow condensation, part II: Criteria for negating influence of gravity, Int. J. Heat Mass Transfer 106 (2017) 313–328, doi: 10.1016/j.ijheatmasstransfer.2016.07.019.

[68] J.E. Galloway, I. Mudawar, CHF mechanism in flow boiling from a short heated wall—I. Examination of near-wall conditions with the aid of photomicrography and high-speed video imaging, Int. J. Heat Mass Transfer 36 (10) (1993) 2511–2526, doi: 10.1016/S0017-9310(05)80190-5.

[69] J.E. Galloway, I. Mudawar, CHF mechanism in flow boiling from a short heated wall—II. Theoretical CHF model, Int. J. Heat Mass Transfer 36 (10) (1993) 2527–2540, doi: 10.1016/S0017-9310(05)80191-7.

[70] H. Lamb, Hydrodynamics, 6th ed., Dover Publications, New York, NY, USA, 1945.

[71] L.M. Milne-Thompson, Theoretical Hydrodynamics, 4th ed., Collier-Macmillan, New York, NY, USA, 1960.

[72] M.S. Bhatti, R.K. Shah, Turbulent and transition flow convective heat transfer in ducts, in: S. Kakac, R.K. Shah, W. Aung (Eds.), Handbook of Single-Phase Convective Heat Transfer, Wiley-Interscience, New York, NY, USA, 1987.

Table 1 Key dimensions of test module (FBM).

Upstream development length, L_d	327.7 mm
Heated length, L_h	114.6 mm
Downstream exit length, L_e	60.7 mm
Thermocouple locations (7) from heated section start, z_{tc}	5.4, 22.7, 40.0, 57.3, 74.6, 91.9, 109.2 mm
Channel height (unheated), H	5.0 mm
Channel width (heated), W	2.5 mm

Table 2 Measurement uncertainties.

Measured Parameters	**Maximum Uncertainty**
Temperature (thermocouples)	±0.5°C
Temperature (RTDs)	±0.5°C
Pressure	±0.7 kPa
FBM heater power	±0.3% reading
Preheater power	±0.6% reading
Mass flow rate	±0.6% reading

Table 3 Summary of key parameters of MST steady-state database for saturated inlet.

	Single-sided Heating	**Double-sided Heating**
Mass velocity, G	429.98 – 1600.04 kg/m^{2}s	379.87 – 2400.00 kg/m^{2}s
Mass flowrate, $\dot{m}$	5.37 – 20.00 g/s	4.75 – 30.00 g/s
Inlet pressure, p_{in}	119.94 – 161.93 kPa	119.61 – 179.23 kPa
Inlet temperature, T_{in}	65.71 – 76.90˚C	66.29 – 79.54˚C
Inlet quality, $x_{e,in}$	0.018 – 0.519	0.011 – 0.405
Wall heat flux, q''_w	1.79 – 29.70 W/cm^2	1.77 – 28.69 W/cm^2
Outlet pressure, p_{out}	113.60 – 159.80 kPa	112.60 – 159.39 kPa
Outlet temperature, T_{out}	59.53 – 70.56˚C	59.00 – 70.33˚C
Outlet quality, $x_{e,out}$	0.070 – 0.607	0.047 – 0.613
Local wall temperature, $T_{wa,z}$	61.67 – 120.51°C (heated) 59.93 – 70.71°C (unheated)	61.49 – 113.77°C

Table 4 Summary of the consolidated saturated-inlet FBCE-CHF database.

Heating		***N***	***G*** **[kg/m²s]**	$\dot{m}$ **[g/s]**	p_{in} **[kPa]**	T_{in} **[°C]**	$x_{e,in}$	p_{out} **[kPa]**	T_{out} **[°C]**	$x_{e,out}$	q''_{CHF} **[W/cm²]**
Single-sided	Horizontal flow; bottom wall heated	31	192.52 – 1592.90	2.41 – 19.91	115.28 – 183.18	54.44 – 76.87	0.004 – 0.633	113.92 – 159.11	59.89 – 67.74	0.049 – 0.780	11.31 – 25.96
	Horizontal flow; top wall heated	31	194.89 – 1600.96	2.44 – 20.01	114.17 – 179.91	57.36 – 77.29	0.003 – 0.658	113.24 – 158.13	56.56 – 67.26	0.044 – 0.720	3.76 – 25.21
	Vertical upflow	38	193.07 – 1631.91	2.41 – 20.40	110.33 – 181.75	56.19 – 79.10	0.004 – 0.686	108.02 – 158.80	58.00 – 70.56	0.039 – 0.794	8.38 – 29.89
	Vertical downflow	31	199.34 – 1626.63	2.49 – 20.33	119.38 – 182.29	58.88 – 80.60	0.011 – 0.668	114.83 – 154.38	59.66 – 66.52	0.044 – 0.766	6.48 – 23.09
	Overall	131	192.52 – 1631.91	2.41 – 20.40	110.33 – 183.18	54.44 – 80.60	0.003 – 0.686	108.02 – 159.11	56.56 – 70.56	0.039 – 0.794	3.77 – 29.89
Double-sided	Horizontal flow	35	183.49 – 158.83	2.29 – 19.81	115.19 – 221.04	52.05 – 78.75	0.013 – 0.635	113.61 – 215.65	56.23 – 78.27	0.097 – 0.781	4.05 – 23.15
	Vertical upflow	42	197.13 – 1587.23	2.46 – 19.84	109.71 – 229.32	52.79 – 80.00	0.008 – 0.678	106.93 – 223.68	58.99 – 79.62	0.098 – 0.901	8.82 – 30.08
	Vertical downflow	32	200.97 – 1604.47	2.51 – 20.06	108.06– 231.32	42.13 – 81.30	0.009 – 0.656	108.47 – 225.66	55.86 – 79.00	0.089 – 0.866	8.26 – 28.76
	Overall	109	183.49 – 1604.47	2.29 – 20.06	108.06 – 231.32	42.13 – 81.30	0.008 – 0.678	106.93 – 225.66	55.86 – 76.62	0.089 – 0.901	4.05 – 30.08
Overall		240	183.49 – 1631.91	2.29 – 20.40	108.06 – 231.32	42.13 – 81.30	0.003 – 0.686	106.93 – 225.66	55.86 – 76.62	0.039 – 0.901	3.77 – 30.08

Table 5 Summary of equations used in the interfacial lift-off model for single-sided heating. Adapted from [48].

Conservation of momentum

$$G^2\frac{d}{dz}\left[\frac{x_{co}^{\ 2}}{\rho_g\alpha_{co}}\right]=-\alpha_{co}\frac{dp}{dz}\pm\frac{\tau_{i,co}P_{i,co}}{A}-\rho_g\alpha_{co}gsin\theta;\quad G^2\frac{d}{dz}\left[\frac{x_1^2}{\rho_g\alpha_1}\right]=-\alpha_1\frac{dp}{dz}-\frac{\tau_{w,g1}P_{w,g1}}{A}\pm\frac{\tau_{i1}P_{i1}}{A}-\rho_g\alpha_1 g\sin\theta$$

$$G^2\frac{d}{dz}\left[\frac{\left(1-x_{co}-x_1\right)^2}{\rho_f\left(1-\alpha_{co}-\alpha_1\right)}\right]=-\left(1-\alpha_{co}-\alpha_1\right)\frac{dp}{dz}-\frac{\tau_{w,f}P_{w,f}}{A}\mp\frac{\tau_{i,co}P_{i,co}}{A}\mp\frac{\tau_{i1}P_{i1}}{A}-\rho_f\left(1-\alpha_{co}-\alpha_1\right)gsin\theta$$

Local velocity

$$u_{co}=\frac{x_{co}G}{\rho_g\alpha_{co}};\qquad u_{g1}=\frac{x_1G}{\rho_g\alpha_1};\qquad u_f=\frac{\left(1-x_{co}-x_1\right)G}{\left(1-\alpha_{co}-\alpha_1\right)\rho_f}$$

Wall shear stress [72]

$$\tau_{w,k}=\frac{1}{2}\rho_k u_k f_k$$

Wall friction factor

$$f_k=C_1+\frac{C_2}{Re_k^{1/C_3}}$$

Phase Reynolds number

$$Re_k=\frac{\rho_k u_k D_k}{\mu_k}$$

Friction factor constants

for laminar flow ($Re_k\le 2100$): $C_1=0\,;C_2=16\,;C_3=1$

for transitional flow ($2100<Re_k\le 4000$): $C_1=0.0054\,;C_2=2.3\times10^{-8}\,;C_3=-2/3$

for turbulent flow ($Re_k>4000$): $C_1=0.00128\,;C_2=0.1143\,;C_3=3.2154$

Interfacial shear stress [69]

$$\tau_{ico}=C_{f,i}\rho_g\left(u_{co}-u_f\right)^2;\qquad \tau_{i1}=C_{f,i}\rho_g\left(u_{g1}-u_f\right)^2;\qquad C_{f,i}=0.5$$

Conservation of energy

$$\frac{dx_{co}}{dz}=0;\qquad \frac{dx_1}{dz}=\frac{q''_wW}{GAh_{fg}}$$

Critical wavelength

$$k_{c1}=\frac{2\pi}{\lambda_{c1}}=\frac{\rho''_f\rho''_{g1}\left(u_{g1}-u_f\right)^2}{2\sigma\left(\rho''_f+\rho''_{g1}\right)}+\sqrt{\left[\frac{\rho''_f\rho''_{g1}\left(u_{g1}-u_f\right)^2}{2\sigma\left(\rho''_f+\rho''_{g1}\right)}\right]^2+\frac{\left(\rho_f-\rho_g\right)g_{n1}}{\sigma}};$$

$$\rho"_{g1}=\rho_g\coth(k_{c1}\delta_1);\quad \rho"_f=\rho_f\coth(k_{c1}\varepsilon);\quad g_{n1}=g\cos\theta$$

Lift-off criteria

$$q''_{CHF}=\rho_g h_{fg}\left(1-x_{e,in}\right)\left[\frac{4\pi\sigma b}{\rho_g}\sin\left(\pi b\right)\right]^{\frac{1}{2}}\left.\frac{\delta_1^{1/2}}{\lambda_{c1}}\right|_{z^*};\quad b=0.2$$

Table 6 Summary of operating conditions used as input for CHF model, predicted CHF values with corresponding critical wavelengths, and statistics of predictions.

Heating	**Orientation**	***N***	***G*** **[kg/m^{2}s]**	p_{in} **[kPa]**	T_{in} **[°C]**	$x_{e,in}$	$q''_{CHF,pred}$ **[W/cm^2]**	λ_c **[mm]**	***MAE*** **[%]**	ξ_{30} **[%] (±30%)**	ξ_{15} **[%] (±15%)**
Single-sided	Horizontal Bottom	15	779.95 – 1592.90	120.99 – 183.18	63.16 – 76.87	0.004 – 0.400	13.92 – 27.64	1.26 – 2.77	9.55	100.00	73.33
	Horizontal Top	15	785.87 – 1600.96	118.53 – 179.91	62.48 – 77.29	0.003 – 0.404	12.92 – 21.58	1.31 – 3.21	13.03	93.33	73.33
	Up	21	789.89 – 1631.91	123.50 – 181.75	63.64 – 79.10	0.004 – 0.518	13.39 – 23.50	1.07 – 2.99	11.56	85.71	76.19
	Down	15	780.77 – 1626.63	119.91 – 182.29	61.50 – 80.60	0.011 – 0.440	12.59 – 20.68	1.21 – 4.32	5.94	100.00	100.00
	Overall	66	779.95 – 1631.91	118.53 – 183.18	61.50 – 80.60	0.003 – 0.518	12.59 – 27.64	1.07 – 4.32	10.16	95.45	81.81
Double-sided	Horizontal	16	777.42 – 1584.83	124.55 – 221.04	63.34 – 78.68	0.013 – 0.392	12.18 – 18.06	1.57 – 6.40	15.92	93.75	50.00
	Up	22	500.03 – 1587.23	128.52 – 229.32	64.92 – 80.00	0.008 – 0.404	12.00 – 27.64	1.44 – 2.95	14.63	81.81	59.09
	Down	14	771.72 – 1604.47	124.53 – 231.32	62.47 – 81.30	0.015 – 0.405	12.35 – 20.96	1.42 – 5.06	11.80	85.71	78.57
	Overall	52	500.03 – 1604.47	124.53 – 231.32	62.47 – 81.30	0.008 – 0.405	12.00 – 27.64	1.42 – 6.40	14.27	86.54	61.54
Overall		118	500.03 – 1631.91	118.53 – 231.32	61.50 – 81.30	0.003 – 0.518	12.00 – 27.64	1.07 – 6.40	11.97	91.53	72.88

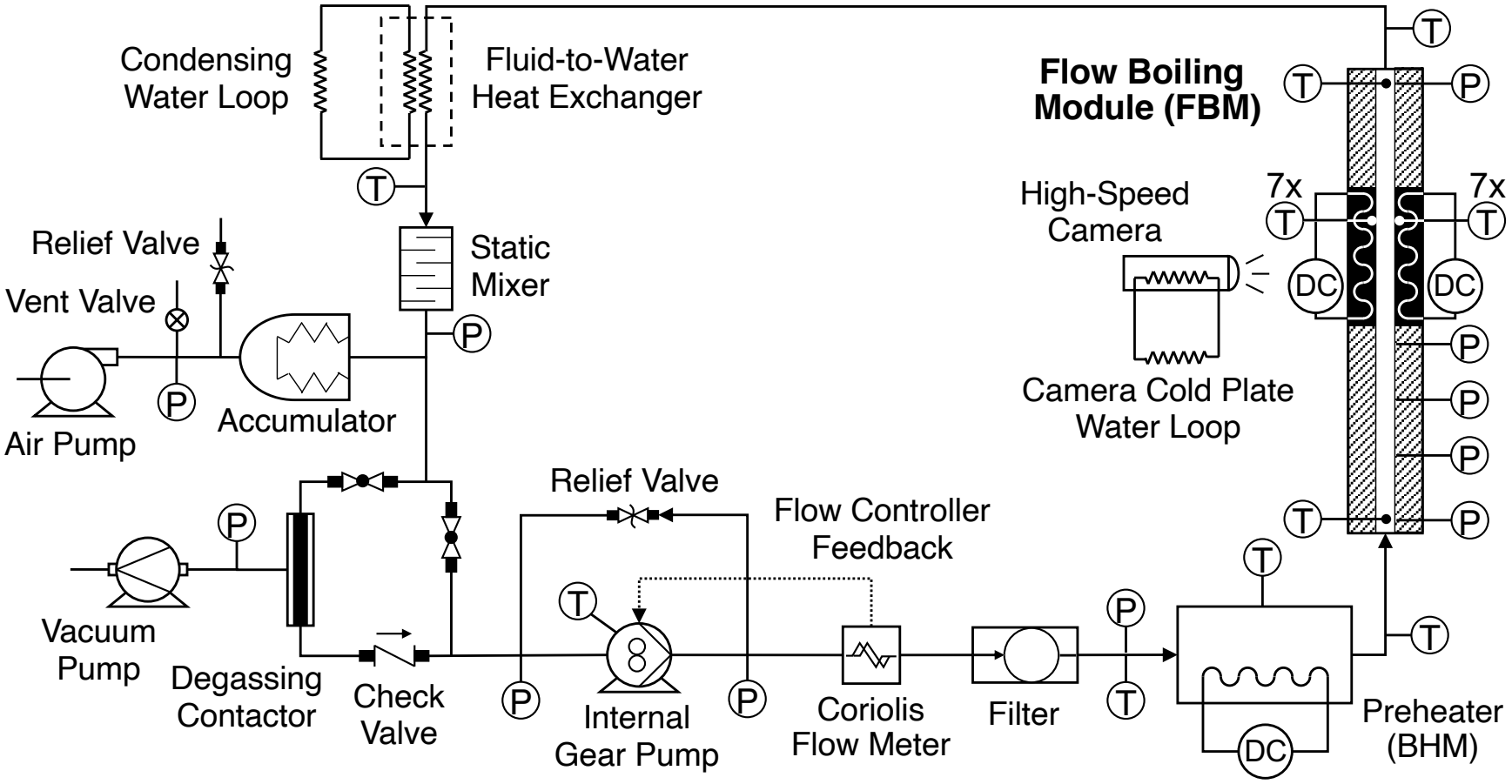

Fig. 1 Schematic diagram of experimental two-phase flow loop.

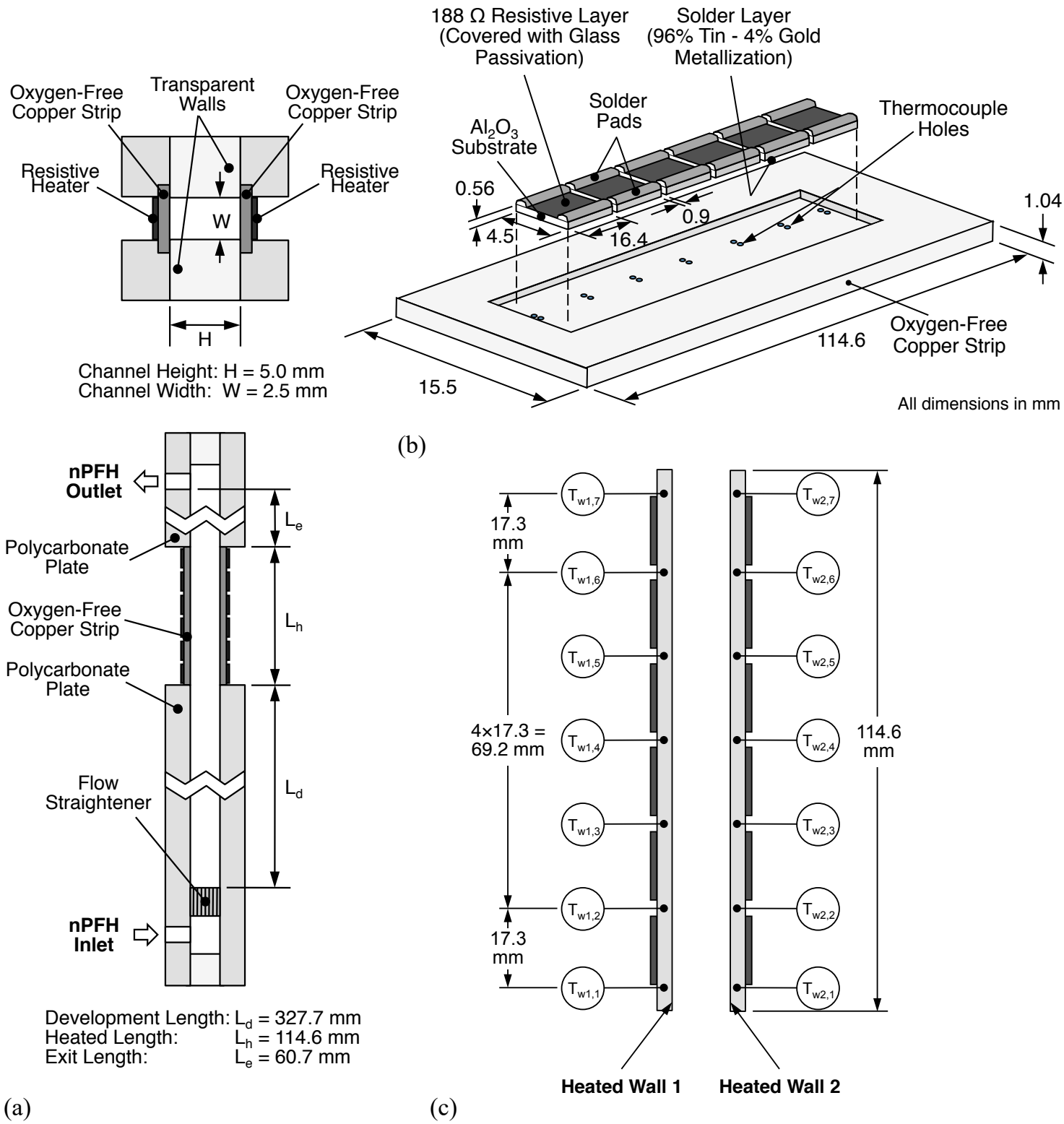

Fig. 2 Schematic representations of (a) overall construction of Flow Boiling Module (FBM), (b) construction of heating strips, and (c) designation of heated walls and local wall temperatures.

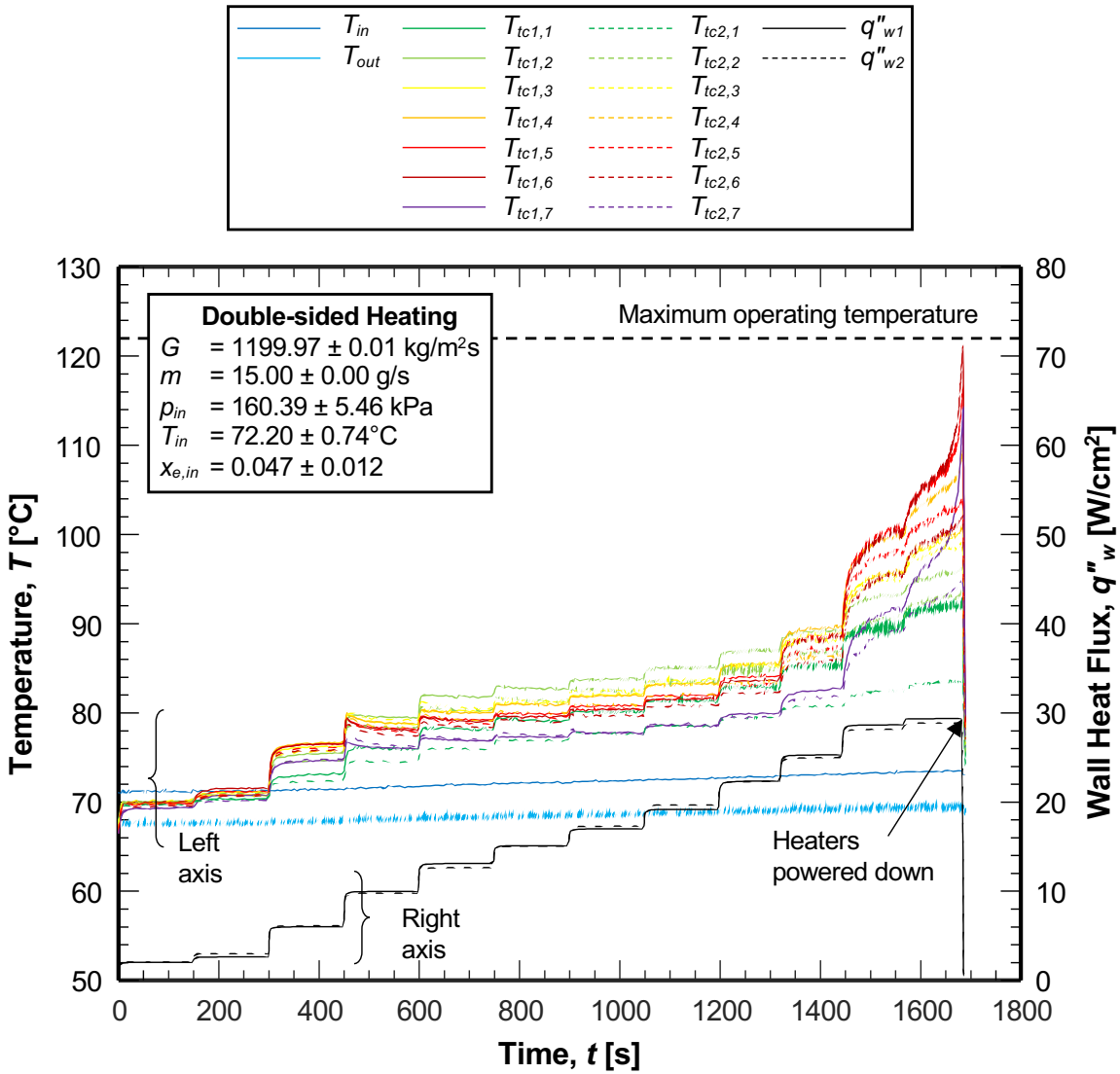

Fig. 3 Temporal variations of fluid inlet, fluid outlet, and heated-strip temperatures for heat flux increments until CHF for a set of operating conditions.

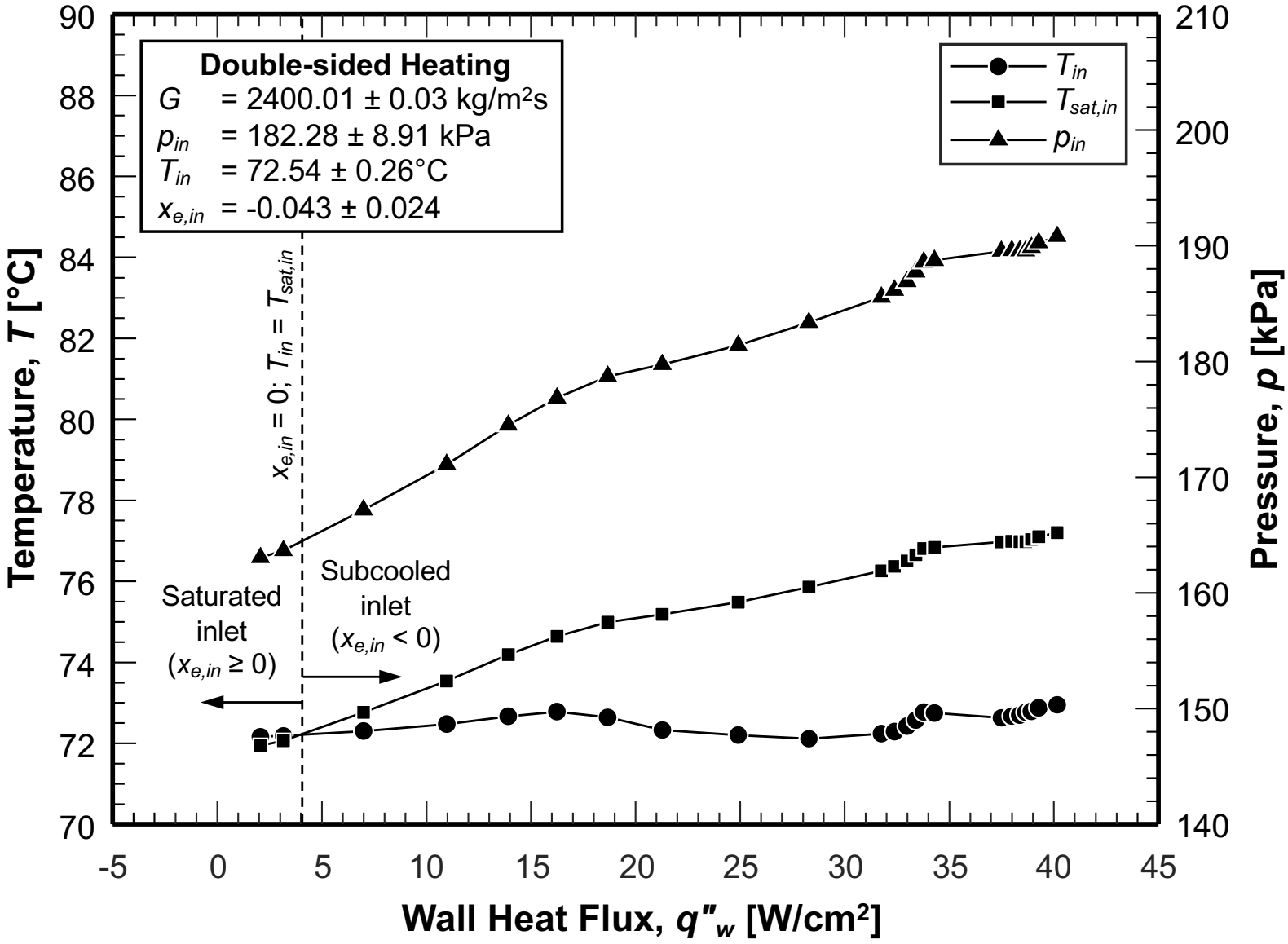

Fig. 4 Variations of measured fluid temperature, measured pressure, and corresponding saturation temperature at FBM heated section inlet with increasing heat flux until CHF for a set of operating conditions.

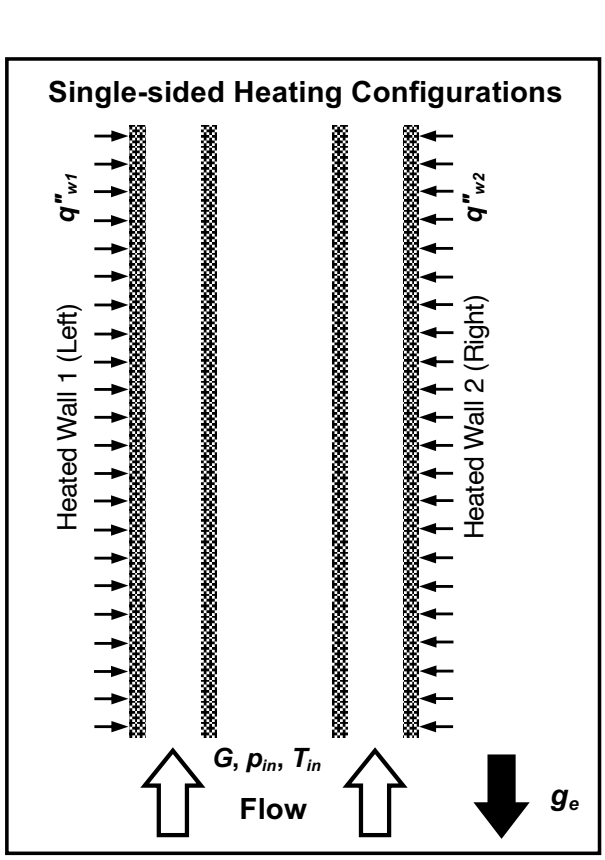

(a)

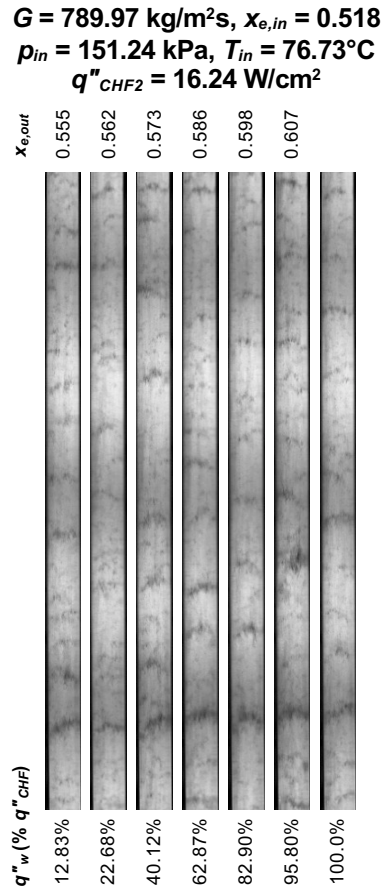

(b)

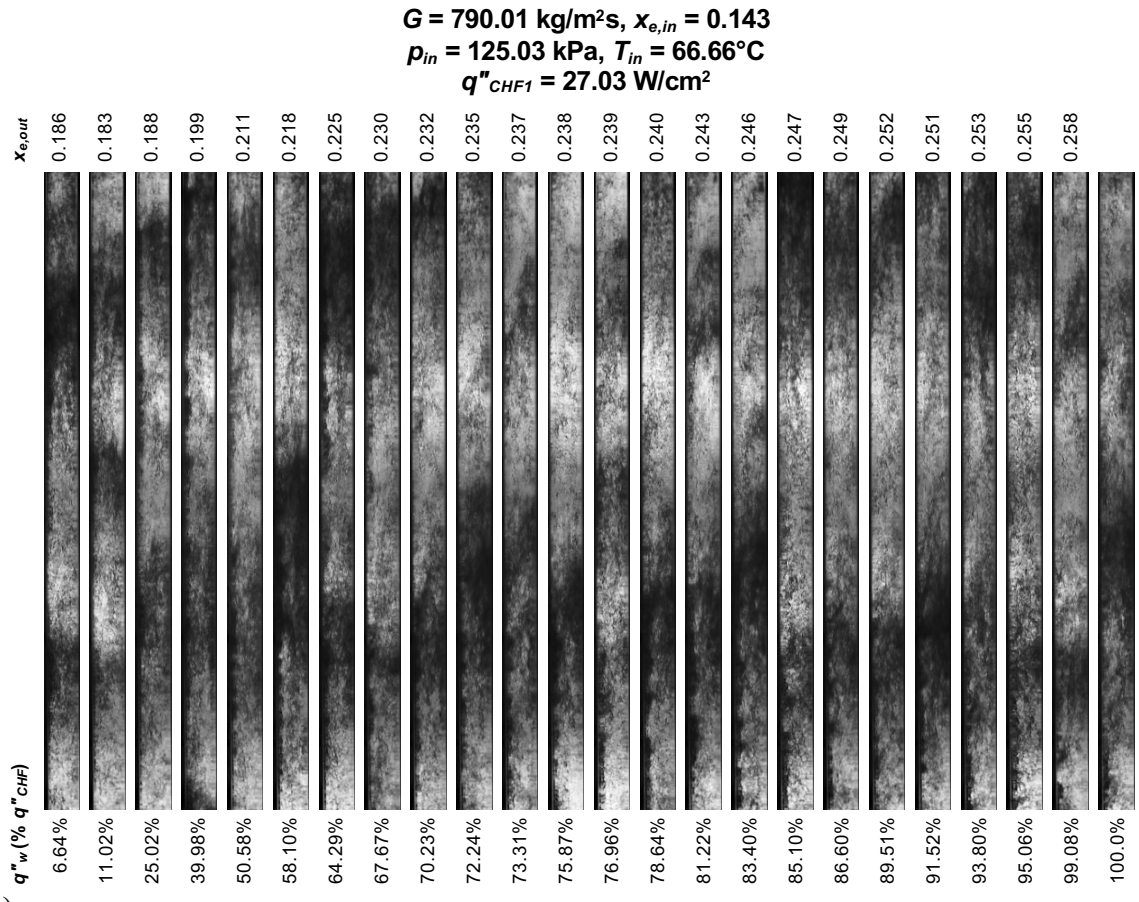

(c)

Fig. 5 (a) Schematic representation of single-sided heating configurations. Flow patterns along the boiling curve until CHF for saturated inlet qualities of $x_{e,in}$ = (b) 0.518 with right wall heated and (c) 0.143 with left wall heated at a mass velocity of $G \approx 790$ kg/m^{2}s. Note that the inlet pressures are different.

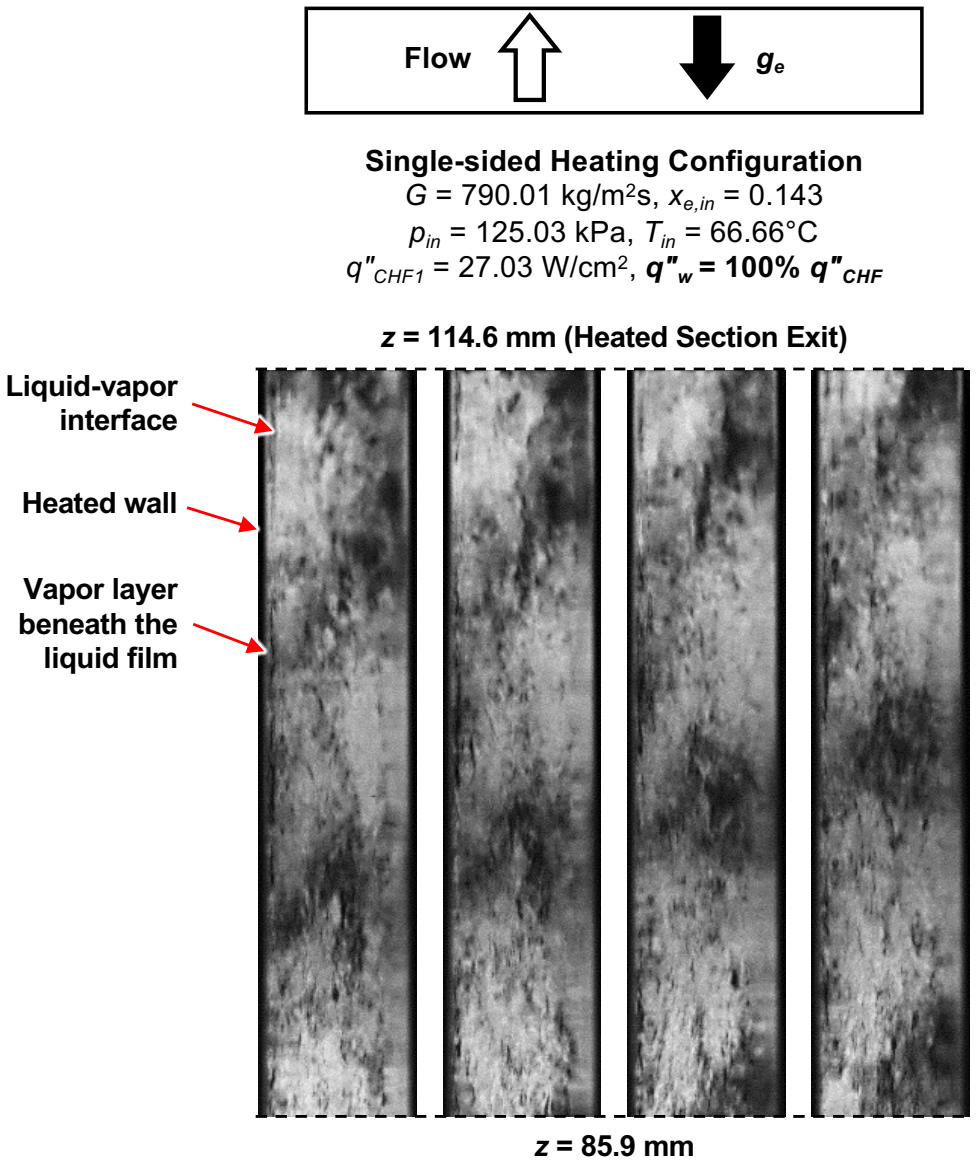

Fig. 6 Flow visualization image sequence at CHF for single-sided (left wall) heating, zoomed-in over the downstream portion of the channel. Note the thin vapor layer next to the left heated wall. Time interval between successive images is 0.5 ms.

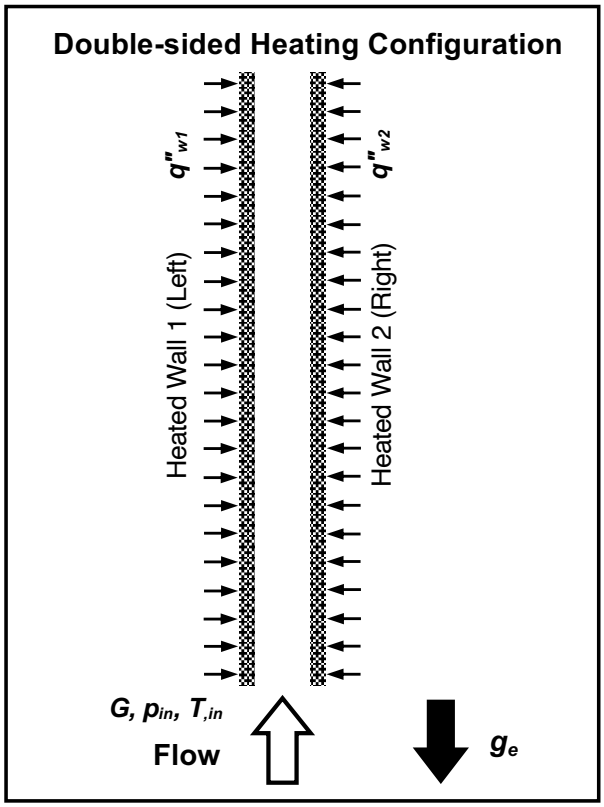

(a)

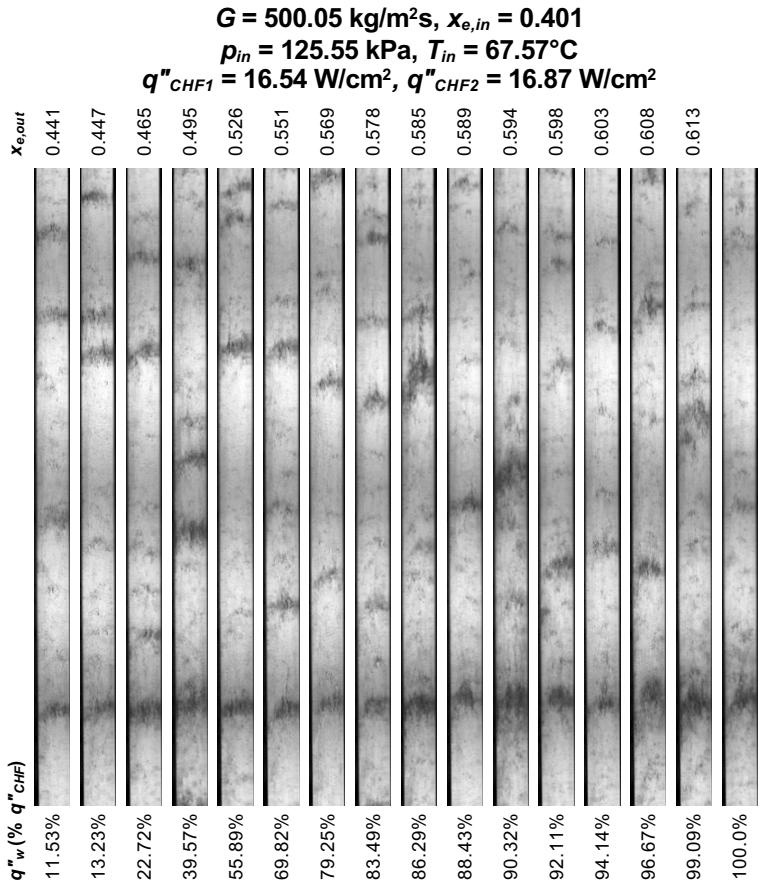

(b)

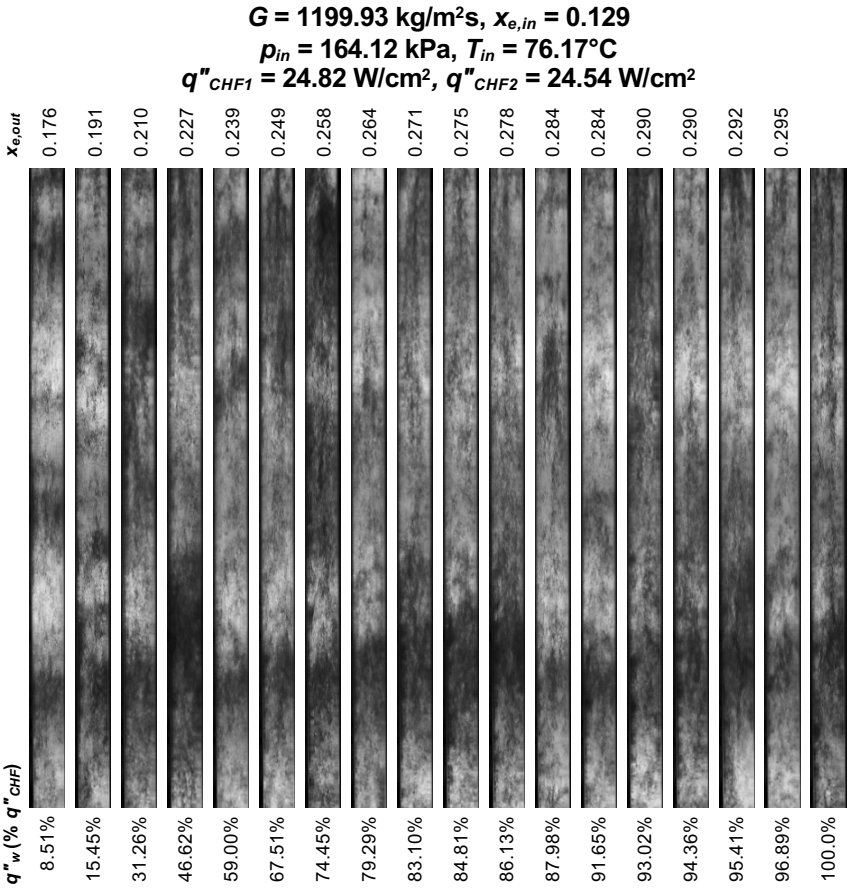

(c)

Fig. 7 (a) Schematic representation of double-sided heating configuration. Flow patterns along the boiling curve until CHF for saturated inlet qualities of $x_{e,in}$ = (b) 0.401 at $G \approx 500$ kg/m²s and (c) 0.129 at $G \approx 1200$ kg/m²s. Note that the inlet pressures are different.

Double-sided Heating Configuration

G = 500.05 kg/m^{2}s, $\boldsymbol{x_{e,in}}$ **= 0.401**, p_{in} = 125.55 kPa, T_{in} = 67.57°C

q''_{CHF1} = 16.54 W/cm^2, q''_{CHF2} = 16.87 W/cm^2

$\boldsymbol{q''_w}$ **= 11.53%** $\boldsymbol{q''_{CHF}}$, $x_{e,out}$ = 0.441

$\boldsymbol{q''_w}$ **= 96.67%** $\boldsymbol{q''_{CHF}}$, $x_{e,out}$ = 0.608

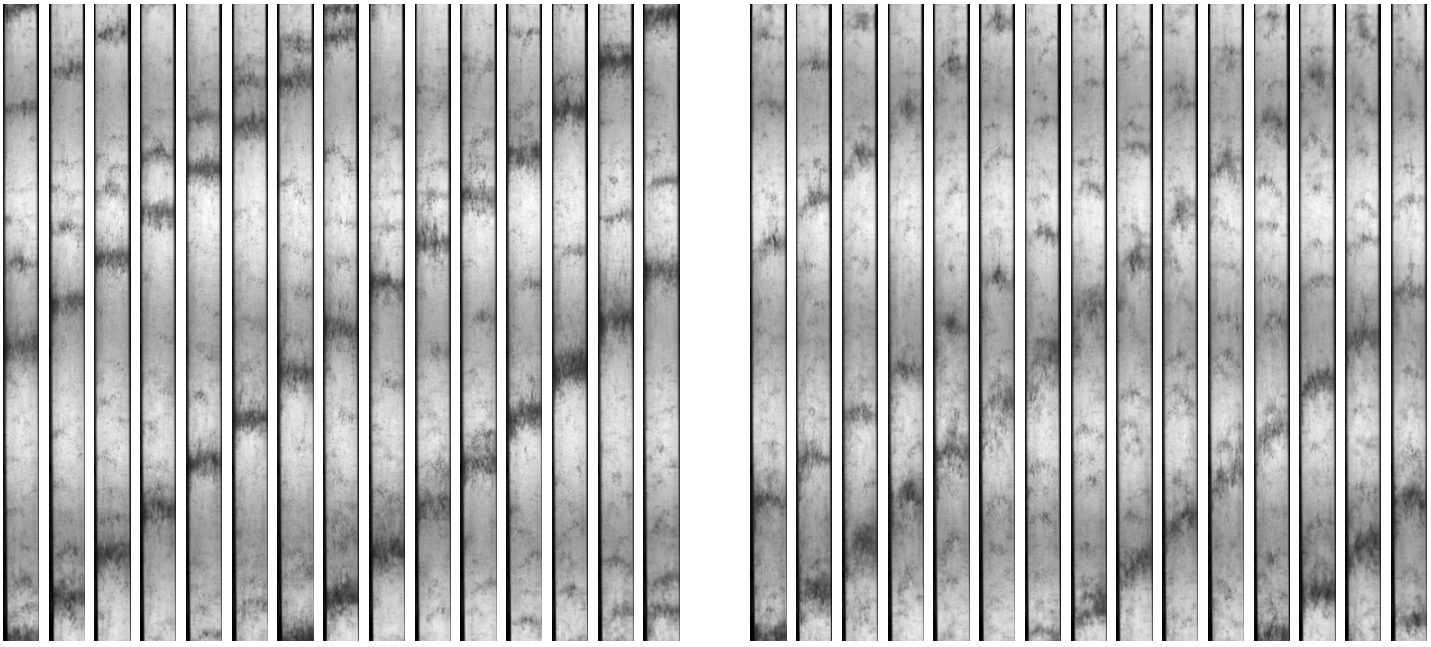

(a)

Single-sided Heating Configuration

G = 789.97 kg/m^{2}s, $\boldsymbol{x_{e,in}}$ **= 0.518**, p_{in} = 151.24 kPa, T_{in} = 76.73°C

q''_{CHF2} = 16.24 W/cm^2

$\boldsymbol{q''_w}$ **= 12.83%** $\boldsymbol{q''_{CHF}}$, $x_{e,out}$ = 0.555

$\boldsymbol{q''_w}$ **= 95.80%** $\boldsymbol{q''_{CHF}}$, $x_{e,out}$ = 0.607

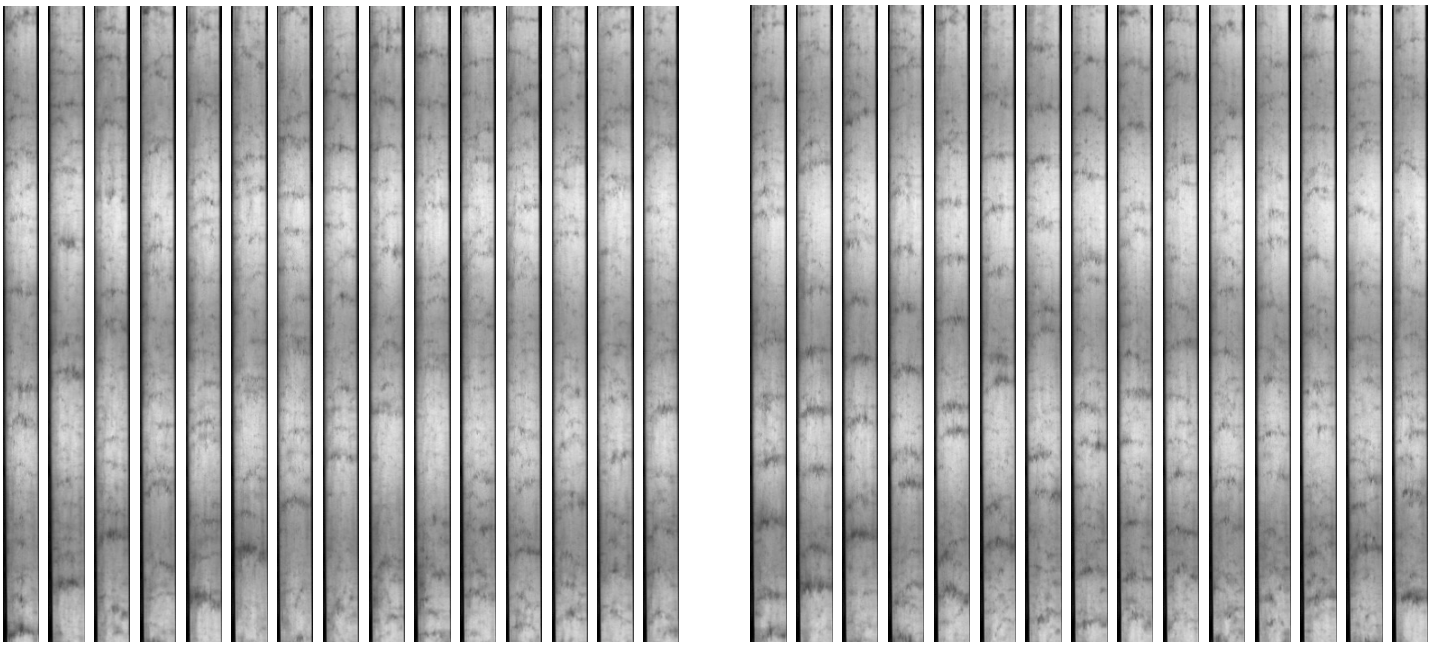

(b)

Fig. 8 Flow visualization image sequences at the heat flux extremes for saturated inlet qualities of $x_{e,in}$ = (b) 0.401 at $G \approx 500$ kg/m^{2}s with double-sided heating and (c) 0.518 at $G \approx 790$ kg/m^{2}s with single-sided heating. Images in each sequence are 2 ms apart.

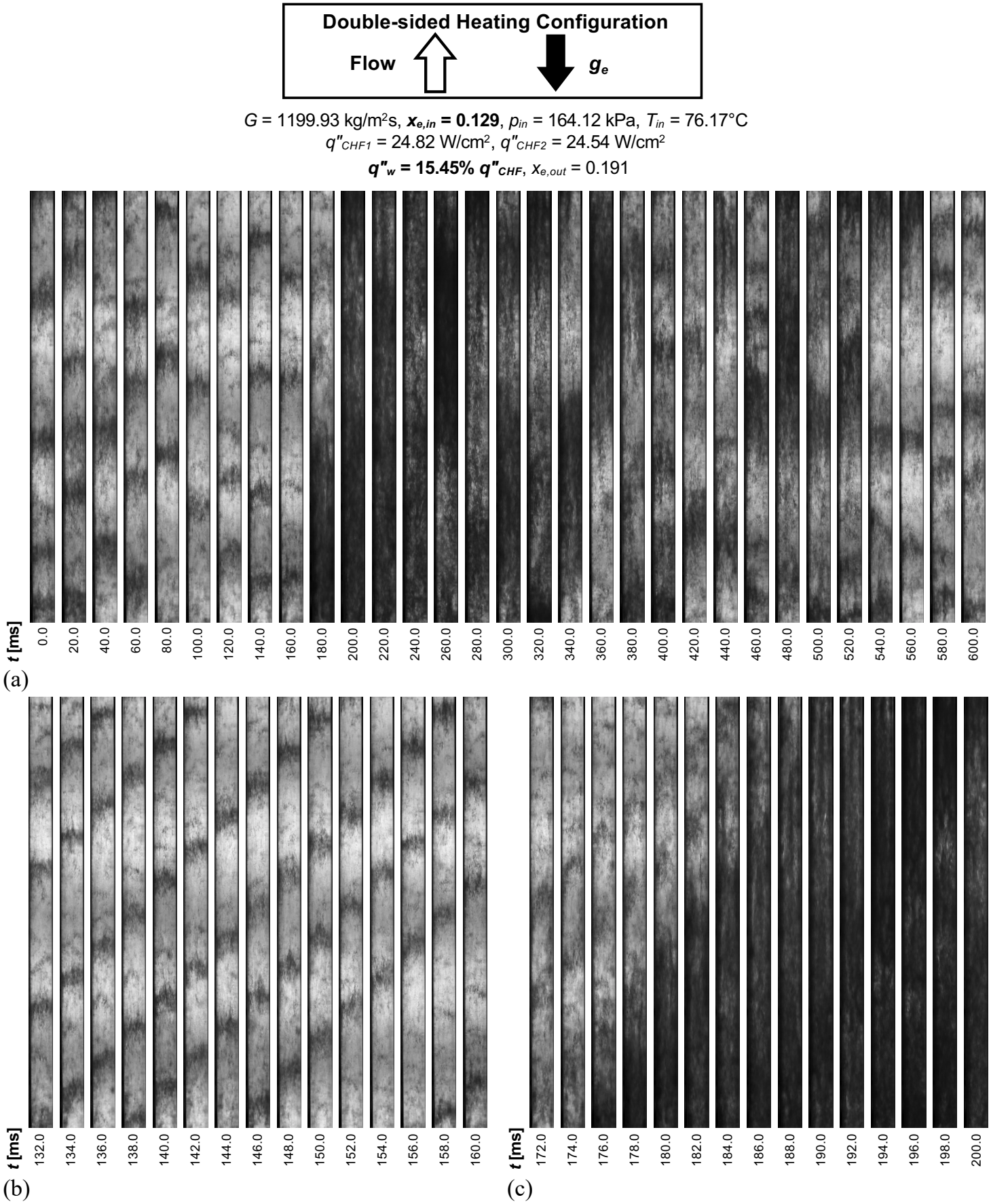

Fig. 9 Flow visualization image sequences for a low saturated inlet quality of $x_{e,in}$ = 0.129 at a heat flux of q''_w = 15.45% q''_{CHF} with double-sided heating: (a) overall behavior over a longer time period, (b) low-density-dominant period, and (c) transition to high-density-dominant period.

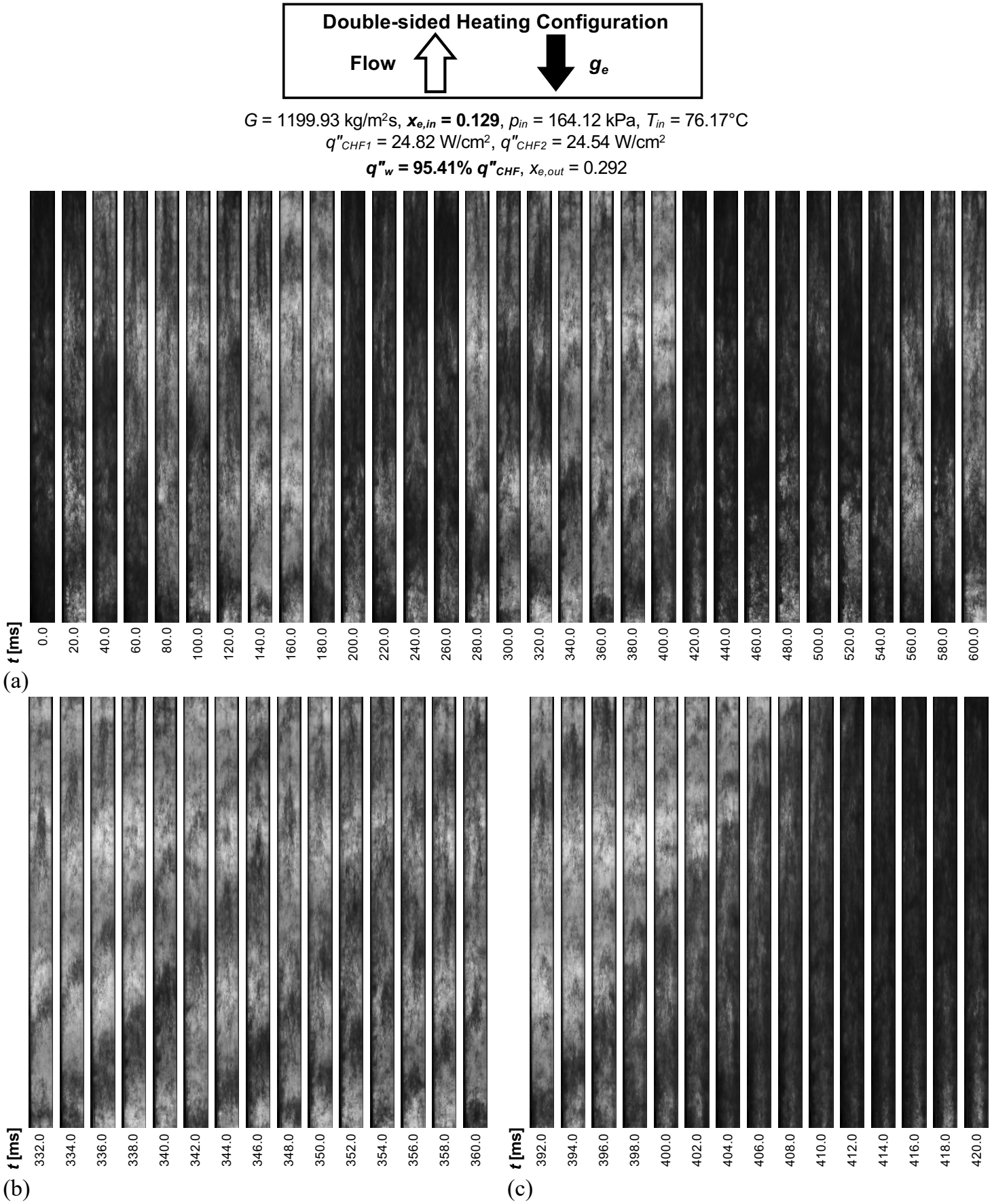

Fig. 10 Flow visualization image sequences for a low saturated inlet quality of $x_{e,in}$ = 0.129 at a heat flux of q''_w = 95.41% q''_{CHF} with double-sided heating: (a) overall behavior over a longer time period, (b) low-density-dominant period, and (c) transition to high-density-dominant period.

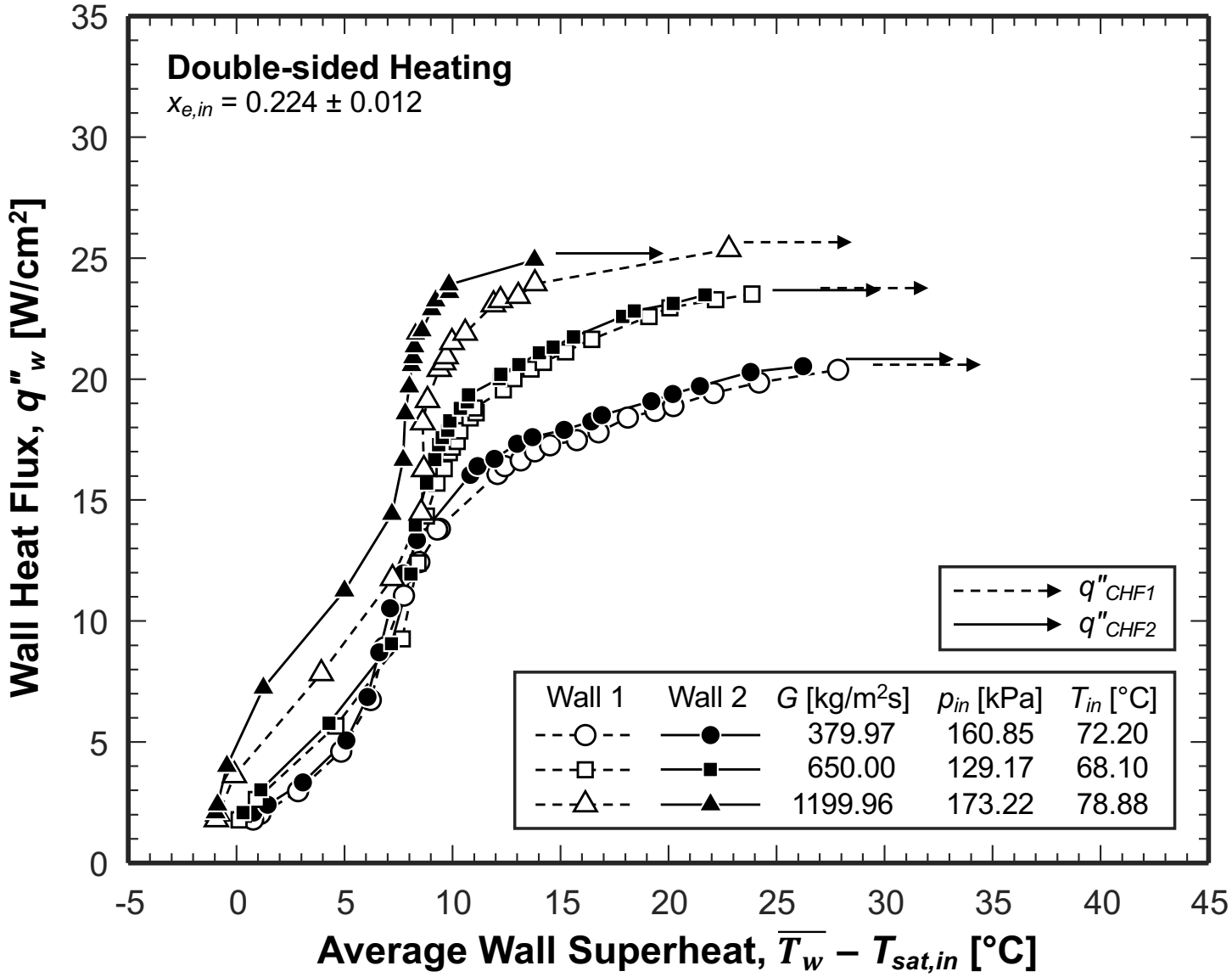

Fig. 11 Boiling curves for double-sided heating configuration at a fixed inlet quality of $x_{e,in} = 0.224$.

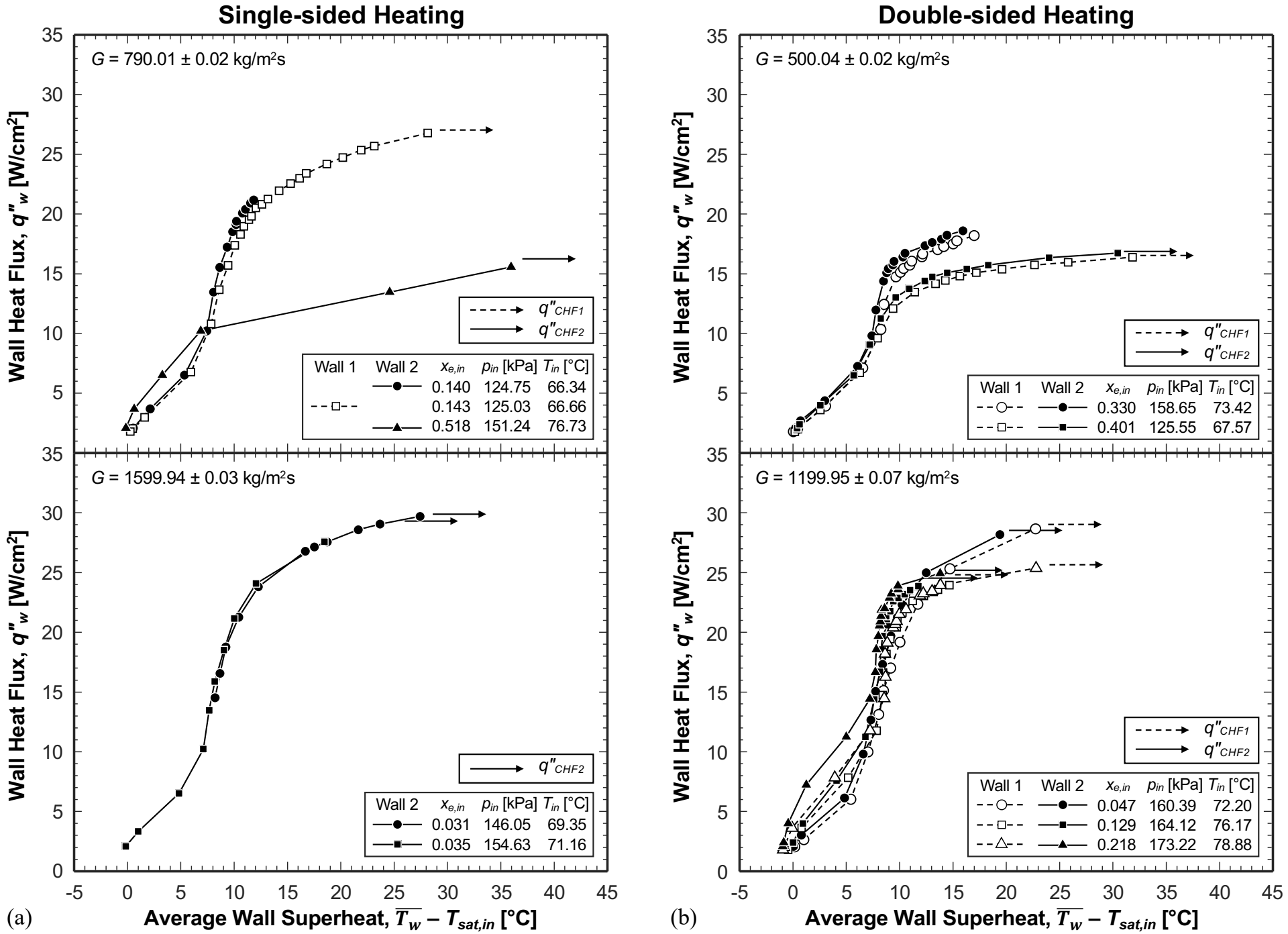

Fig. 12 Boiling curves for both (a) single-sided and (b) double-sided heating configurations at various operating conditions. Mass velocity is constant in each sub-plot.

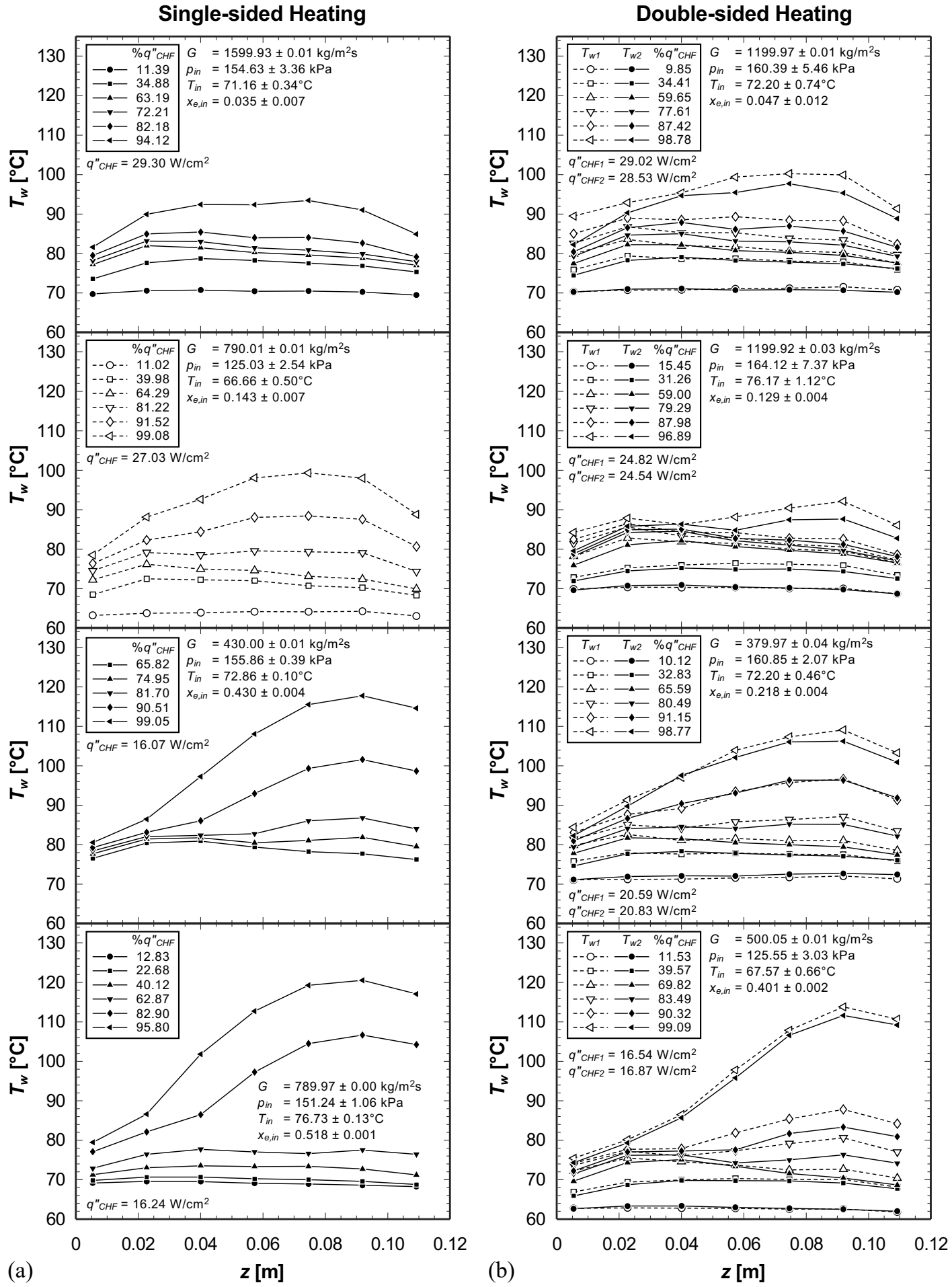

Fig. 13 Streamwise local wall temperature profiles for different heat fluxes with both (a) single-sided and (b) double-sided heating configurations at a variety of operating conditions.

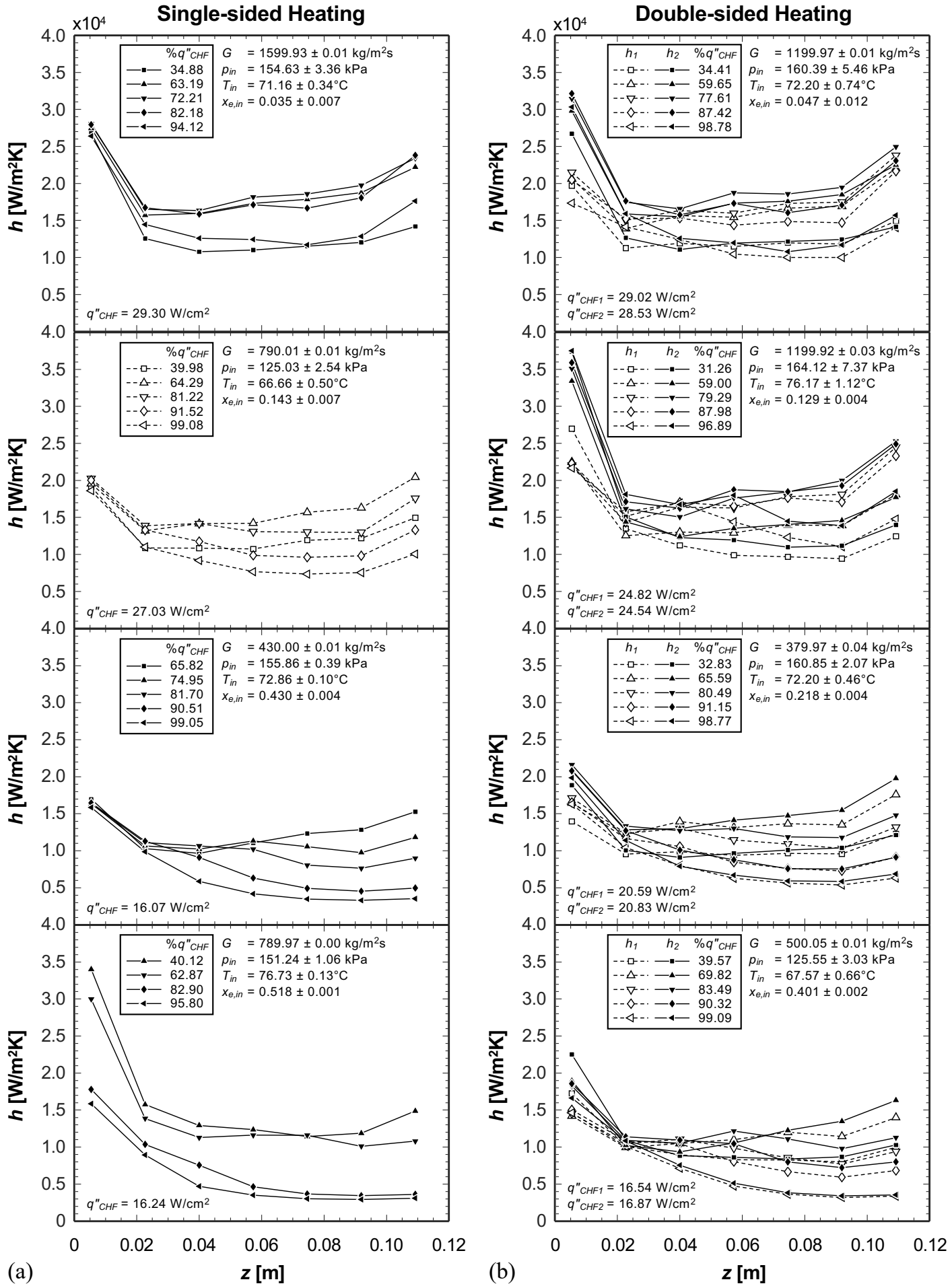

Fig. 14 Streamwise local heat transfer coefficient profiles for different heat fluxes with both (a) single-sided and (b) double-sided heating configurations at a variety of operating conditions.

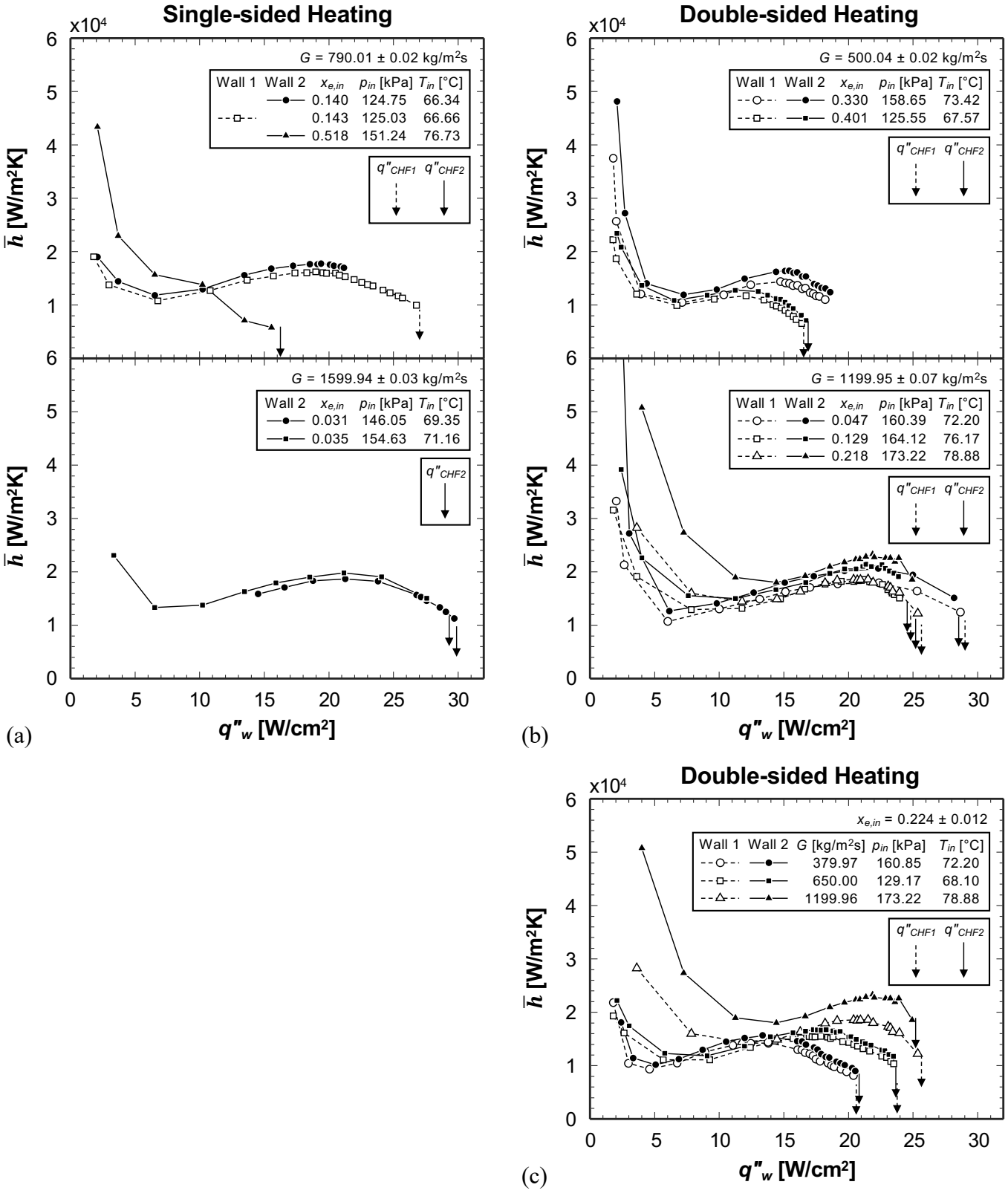

Fig. 15 Average heat transfer coefficient variations with wall heat flux for both (a) single-sided and (b) double-sided heating configurations at fixed mass velocities and (c) double-sided heating at a fixed inlet quality.

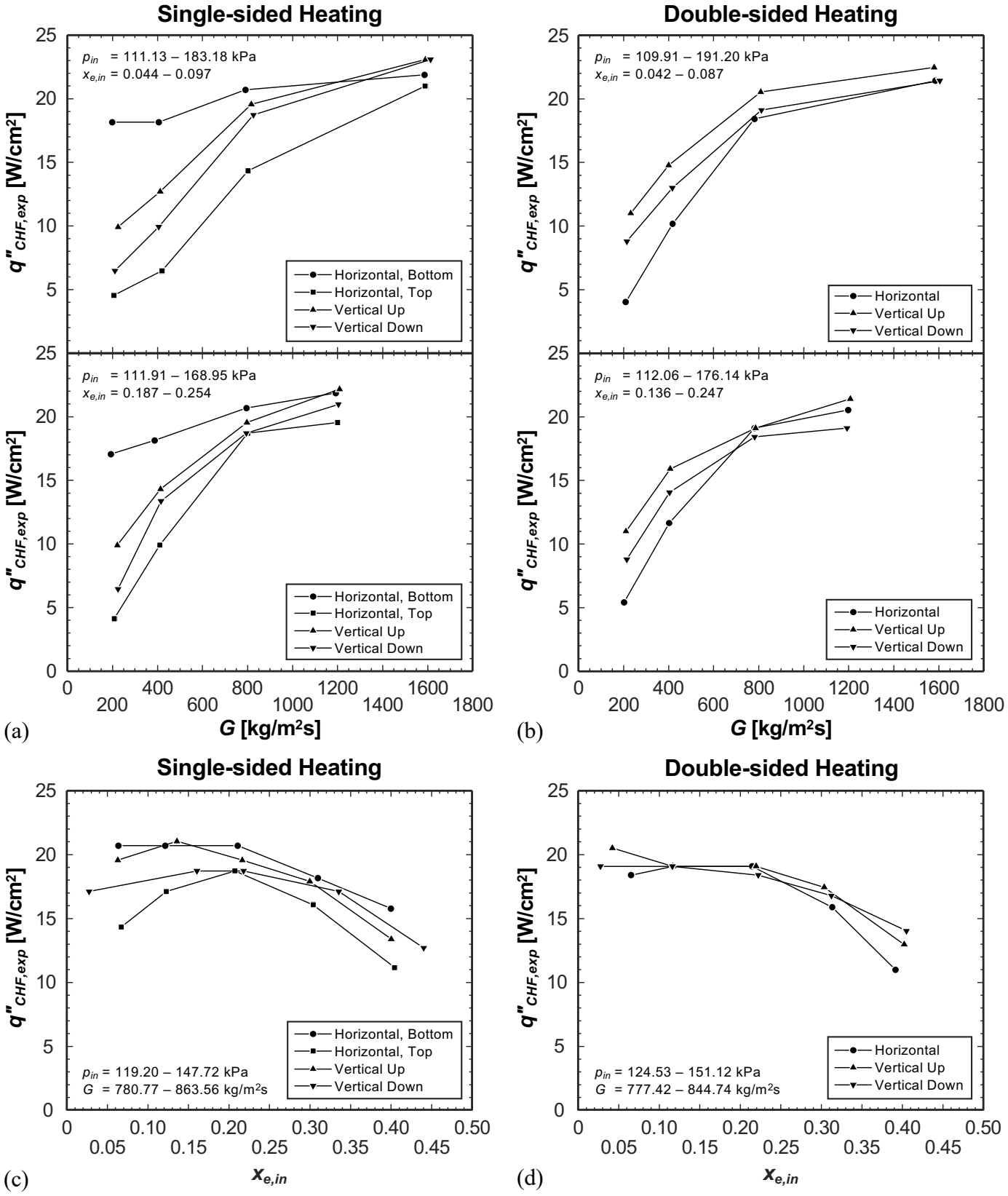

Fig. 16 Experimental CHF variations with respect to mass velocity for both (a) single-sided and (b) double-sided heating, and inlet quality for both (c) single-sided and (d) double sided heating.

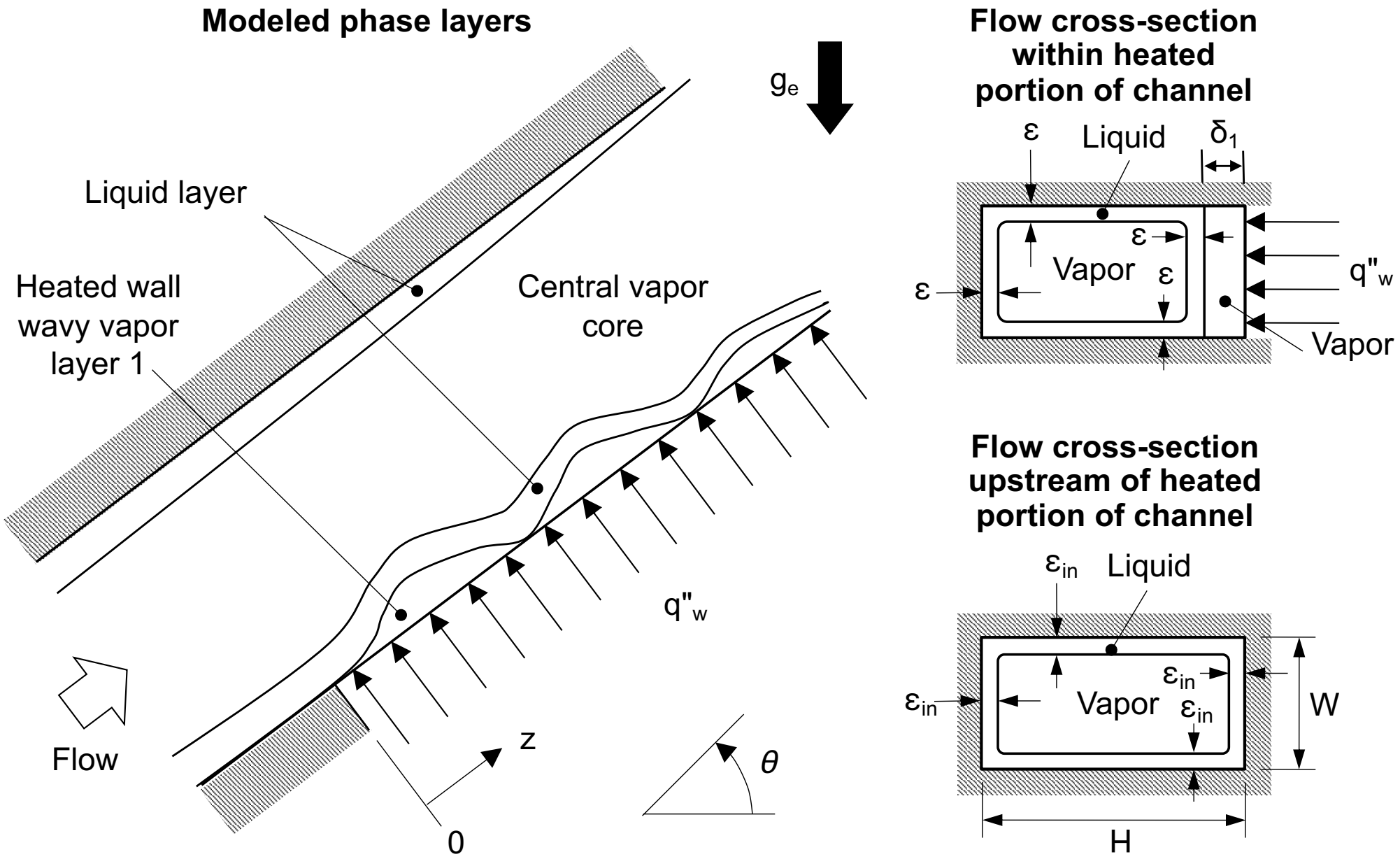

Fig. 17 Schematics of modeled phase layers and channel cross-section used in the interfacial lift-off model. Adapted from Kharangate *et al*. [48].

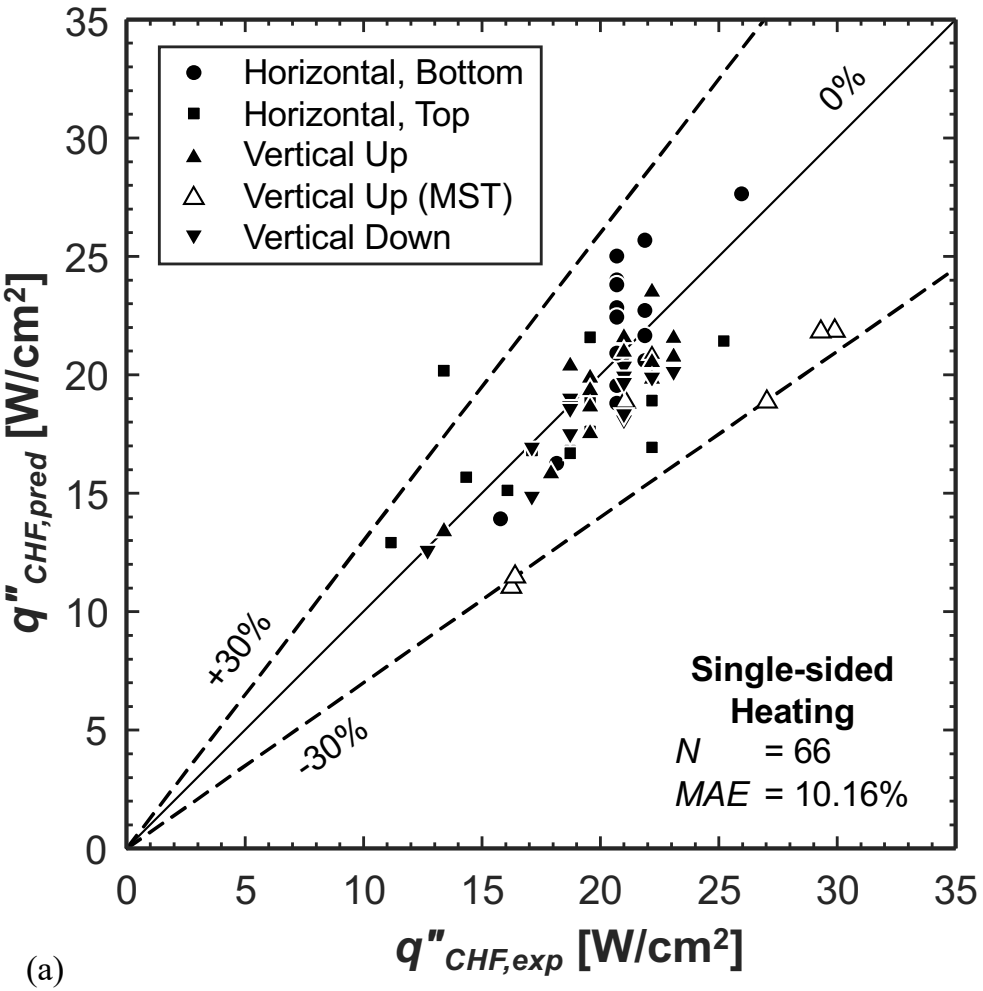

(a)

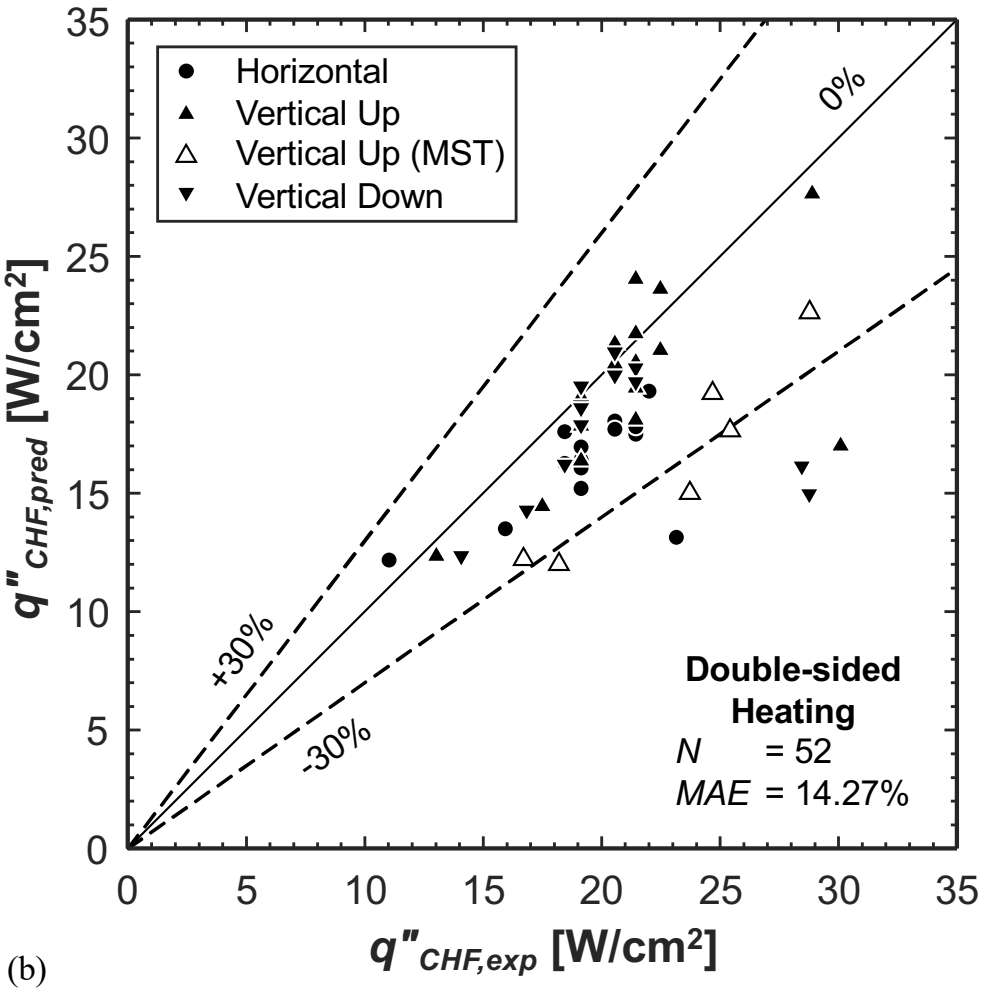

(b)

Fig. 18 Comparison of experimental and predicted CHF values for both (a) single-sided and (b) double-sided heating.